A statistical approach to polarimetric and photometric investigation of the intermediate-age open cluster NGC 1912

Samrat Biswas,[1]★ Biman J. Medhi,[1,2]† Sushmita Deb,[1] Sukanta Deb,[3] H.S. Das,[4] and G.I. Perren[5,6]
[1] *Gauhati University, Gopinath Bordoloi Nagar, Jalukbari, Guwahati 781014 ,Assam,India*
[2] *Aryabhatta Research Institute of Observational Sciences, Manora Peak, Nainital 263129, India*
[3] *Department of Physics, Cotton University, Guwahati 781001, Assam, India*
[4] *Department of Physics, Assam University, Silchar 788011, India*
[5] *Instituto de Física de Rosario (IFIR-CONICET), Rosario (2000), Argentina*
[6] *Facultad de Ciencias Exactas, Ingeniería y Agrimensura (UNR), Rosario (2000), Argentina*

Accepted 2024 June 09. Received 2024 June 05; in original form 2024 March 28

ABSTRACT

This paper presents a comprehensive multi-wavelength investigation of the intermediate-age open cluster NGC 1912. We identified 401 member stars for NGC 1912 using K-nearest neighbour (kNN) and Gaussian Mixture Model (GMM) machine learning techniques. The fundamental parameters determined for the cluster are Metallicity (z) = 0.0141 ± 0.0006, Log(age) = 8.519 ± 0.040, Binary fraction (b_{frac}) = 0.445 ± 0.035, Visual extinction (A_V) = 0.864 ± 0.033 mag, Total-to-selective extinction ratio (R_V) = 3.007 ± 0.096, distance = 1096 ± 15 pc. The central density (ρ_o), core radius (r_c), tidal radius (r_t), and background density (ρ_{bg}) for the cluster are obtained as 0.643 ± 0.067 stars arcmin^{-2}, 7.743 ± 0.784 arcmin, 84.633 ± 7.188 arcmin, and 0.001 ± 0.000 stars arcmin^{-2}, respectively. Dynamical mass segregation study revealed a concentration of some apparently massive stars towards the cluster center. Polarimetric analysis of 90 stars in BVR_cI_c wavelength bands revealed that the observed polarization in NGC 1912 is not solely attributed to interstellar dust. The Galactic magnetic field is dominant in this region. Dust grain sizes within the intra-cluster region are found to be relatively smaller than that of the general ISM. The extinction map revealed the existence of a potential "interstellar bubble" located close to the cluster region. Towards the periphery of the probable bubble region, that displays an ovoid-like geometry, 16 probable young stellar objects (YSOs) have been detected, suggesting the ongoing of triggered secondary star formation events in this region.

Key words: polarization – dust, extinction – ISM: magnetic fields – stars: massive – ISM: bubbles – stars: formation

1 INTRODUCTION

Open star clusters are one of the alluring astrophysical environments that serve as significant probes, offering valuable insights into the intricacies of star formation and evolution. Given that the stars in an open cluster formed in the same interstellar cloud, it is reasonable to infer that they have similar ages, chemical compositions, distances as well as centre-of-mass motion (Friel 1995; Piskunov et al. 2006; Li et al. 2021; Deb et al. 2022).

The initial stages in the study of open clusters involve, the identification of the genuine cluster members amid the presence of both foreground and background stars. It is followed by the determination of the parameters such as cluster mean parallax and proper motion, core and tidal radius, central as well as background density, age, metallicity, distance, extinction and others. Various techniques have been devised to distinguish between cluster members and field stars, relying on either photometry, astrometry, or a combination of both (e.g. Vasilevskis et al. 1958; Sanders 1971; Sarro et al. 2014; Stott 2018; Balaguer-Núñez et al. 2020). Methods rooted in machine learning, including UPMASK (Krone-Martins & Moitinho 2014; Cantat-Gaudin et al. 2018), pyUPMASK (Pera et al. 2021), KMEANS (Sánchez Almeida & Allende Prieto 2013; El Aziz et al. 2016), ANN (Castro-Ginard et al. 2020), KNN (Agarwal et al. 2021; Deb et al. 2022), GMM (Gao 2020; Agarwal et al. 2021; Deb et al. 2022), DBSCAN (Gao 2014; Bhattacharya et al. 2017; Hunt & Reffert 2021), HDBSCAN (Hunt & Reffert 2021, 2023), and RANDOMFOREST (Gao 2018) have also been employed to determine cluster membership.

Over time, the more massive stars of a cluster tend to migrate towards the center, whereas the lower mass stars disperse farther away from the center. This phenomenon, known as dynamical mass segregation, arises as a natural consequence of energy equipartition spurred by two-body interactions (Spitzer Jr 1969; Gao 2019; Raboud & Mermilliod 1998; Noormohammadi et al. 2023). Also, the presence of high mass stars can further induce secondary star formation in the regions of the cluster harbouring gas and dust (Kim et al. 2021). Stellar feedbacks from these massive stars can locally trigger the onset of gravitational collapse leading to what is called triggered star formation (Girichidis et al. 2020). Interstellar matter (ISM) thus play a crucial role in the formation of stars (Bodenheimer 1997; Hirashita & Ferrara 2002; Hirashita, H. & Hunt, L. K. 2004). The study of dust and ISM, therefore, becomes imperative, to understand the fundamental processes involved in the star formation. Polarization

---

★ E-mail: samrat@gauhati.ac.in
† E-mail: bimanjmedhi@gmail.com

due to the ISM serves as an important probe to this study. Due to asymmetric absorption of electromagnetic wave along various axes of magnetically aligned non-spherical dust particles, the background starlight exhibits dichroic polarization (Spitzer Jr & Tukey 1951; Davis Jr & Greenstein 1951; Serkowski 1973; Medhi et al. 2007, 2010; Singh et al. 2020). While the primary mechanism responsible for grain alignment has posed an intriguing challenge in the study of grain dynamics (Lazarian et al. 1997; Lazarian 2003; Voshchinnikov 2012), the prevailing belief is that asymmetric grains typically align themselves with the local magnetic field, with their shortest axis aligning parallel to the magnetic field (Davis Jr & Greenstein 1951). The observation of polarized light at various wavelengths thus provides a great opportunity to study the magnetic fields, dust distribution as well as properties such as the size and shape of dust grains, in the region under consideration (Serkowski 1973).

This work focuses on the investigation of the region within and around the intermediate age open cluster NGC 1912, alternatively known as Messier 38 or Starfish cluster [R.A. (J2000) = $05^h28^m40^s$; Dec. (J2000) = $+35°50'54''$; l = 172°.250; b = 0°.695]. Positioned in the anti-galactic center direction, it is located within the constellation of Auriga (Pandey et al. 2007). Its Trumpler classification is II2r (Subramaniam & Sagar 1999).

Cluster NGC 1912 has not been extensively studied. Some of the previous works are discussed as follows. The work of Subramaniam et al. (1995) suggested that NGC 1912 and NGC 1907 are probable binary cluster. However, N-body simulations by De Oliveira et al. (2002) suggests that NGC 1912 and NGC 1907 were born in different parts of the galaxy. Dias et al. (2002b) introduced an updated NGC 1912 catalog, enhancing the previous compilations by Lyngå (1985). Dias et al. (2002a) carried out membership probability assessments for NGC 1912 based on Tycho2 proper motions, using the statistical method proposed by Sanders (1971). In a recent investigation by Hunt & Reffert (2023), the authors reported 743 cluster members for NGC 1912. They used *Gaia* Data Release 3 (DR3; Gaia Collaboration et al. 2021a, 2023) sources with a limiting magnitude of G < 20 mag. They selected the HDBSCAN algorithm for their membership analysis based on insights from their prior work in Hunt & Reffert (2021), where they conducted a comparative evaluation of various clustering algorithms. Subramaniam & Sagar (1999) carried out CCD photometry for NGC 1912 in B, V and I filters (with a limiting magnitude of V ≈ 20 mag) and reported the distance, reddening and age estimates for the cluster as 1820 pc, 0.23 mag and 250 Myr, respectively. In the investigation led by Kharchenko et al. (2005) the authors reported a distance of 1066 pc, $E(B-V)$ of 0.25 mag, and log(age) = 8.56 for NGC 1912. Their work was based on the data from ASCC-2.5 (Kharchenko 2001), a catalog comprising 2.5 million stars with proper motions in the Hipparcos system and magnitudes in B, V passbands. Griggio et al. (2023) used *Gaia* DR3 data along BaSTI-IAC (Hidalgo et al. 2018) isochrones to report distance ≈ 1130 pc, Age = 300 Myr, $E(B-V)$ = 0.26 and $[Fe/H]$ = 0.06. Other existing literature on NGC 1912 present different values of the cluster parameters : distance (in the range of ≈ 800 pc to 1400 pc), age (≈ 250 Myr to 375 Myr), reddening (≈ 0.24 mag to 0.27 mag) and $[Fe/H]$ (≈ - 0.183 to 0.014) (Johnson et al. 1961; Becker 1963; Hoag & Applequist 1965; Donor et al. 2020; Jacobson et al. 2002; Dias et al. 2021; Spina et al. 2021; Fu et al. 2022; Netopil et al. 2022). Pandey et al. (2007) presented a wide-field CCD photometry of NGC 1912 in B, V, I_c bands, alongside the cluster NGC 1907. The mass function slope for NGC 1912 was reported as −1.12 ± 0.30, and the photometric binary content was determined to be 30 ± 10 per cent within the mass range $1.0 \leq M_\odot \leq 3.1$. Almeida et al. (2023) conducted a study estimating the individual stellar masses (including those within binary systems) for NGC 1912 and 772 other open clusters using *Gaia* Early Data Release 3 (EDR3; Gaia Collaboration et al. 2021b; Lindegren, L. et al. 2021; Riello, M. et al. 2021). The approach involves generating a grid of synthetic clusters and comparing it with the observed cluster data. Furthermore, the authors undertook a thorough investigation of the relationship between masses and other fundamental cluster parameters. Li et al. (2021) conducted an in-depth analysis of light curves spanning approximately 63 hours, derived from the reduction of over 3600 CCD frames in B, V and R filters revealing 24 variable stars in the NGC 1912 cluster. This included 16 periodic variable stars, seven eclipsing binaries, and one star of uncertain classification.

In this study, we conducted a comprehensive statistical analysis of the cluster NGC 1912 across multiple wavelength bands incorporating polarimetric and photometric domains. This work represents the first instance of polarimetric analysis conducted in this cluster. We have reported B, V, R_c and I_c band ($\lambda_{B_{\rm eff}}$ = 0.440 μm, $\lambda_{V_{\rm eff}}$ = 0.550 μm, $\lambda_{R_{\rm eff}}$ = 0.660 μm and $\lambda_{I_{\rm eff}}$ = 0.800 μm) (Das et al. 2013; Deb Roy et al. 2015) polarimetric observations for 90 stars (brighter than $V \simeq 18$ mag) in the direction of NGC 1912. These observations coupled with the extinction studies of the region provided significant insights into the dust properties, contributing to a deeper understanding of the star formation scenario in the region of the cluster. Membership analysis as well as the mass segregation studies of the cluster also played a pivotal role in this respect.

The remaining paper is organized as follows: Section 2 outlines the archival datasets employed. Section 3 deals with the membership analysis of the cluster, determination of the cluster parameters and investigation of the mass segregation effect for the cluster. Section 4 focuses on the polarimetric analysis of the cluster. Section 5 discusses the dust properties in the region within and around the cluster. Section 6 discusses the dust distribution and star formation scenario in the region of the cluster NGC 1912. Finally, the results, summary and discussions are presented in Section 7.

2 ARCHIVAL DATA USED

2.1 *Gaia* Data

We used parallax and proper motion data from *Gaia* DR3 (Gaia Collaboration et al. 2021a, 2023) to estimate the membership probabilities of the stars within the cluster NGC 1912. The individual distances for the polarimetrically analyzed stars were computed using the corresponding parallax values from *Gaia* DR3. Photometric measurements from DR3 were used to estimate metallicity, age, binary fraction, extinction, distance and total-to-selective extinction ratio for the cluster. It was also used to conduct a statistical study of mass segregation within the cluster.

With an improved completeness limit of G = 21 mag *Gaia* DR3 offers access to over 1.468 billion sources with a full 5-parameter astrometric solution. Photometric data cover sources across a magnitude range from G ≈ 21 mag to G ≈ 3 mag. The uncertainties associated with parallax vary from 0.02–0.03 mas for G < 15 mag, to 1.3 mas at G = 21 mag and that for proper motion vary from 0.02 – 0.03 mas $\rm yr^{-1}$ and extend up to 1.4 mas $\rm yr^{-1}$ at G = 21 mag (Gaia Collaboration et al. 2021a; Riello, M. et al. 2021).

Further details regarding the *Gaia* data releases are available at `https://www.cosmos.esa.int/web/gaia`.

All the studies in this paper, concerning the *Gaia* data has been carried out in a photometric magnitude limit of G < 21 mag.

2.2 2MASS NIR JHK_s Data

The point source catalog (PSC) from the Two Micron All Sky Survey (2MASS) provides precise astrometry and photometry for 470,992,970 near-infrared sources across three wavelength bands: J (1.235 μm), H (1.662 μm), and K$_s$ (2.159 μm) (Cutri et al. 2003; Skrutskie et al. 2006). This catalog is derived from scans of 59,731 tiles, covering 99.998 per cent of the sky.

To construct the extinction map of the cluster NGC 1912, we extracted NIR JHK_s data within a square box of side 35 arcmin around the cluster center, from the 2MASS PSC. We imposed the constraint for the photometric quality flag as "AAA" as it exhibits a *S/N* ≥ 10 and a photometric uncertainity ≤ 0.10.

2.3 *Herschel* Data

With its primary objective of observing the "cool universe", Herschel[1] offers groundbreaking observational abilities in the far-infrared and submillimeter range spanning $55-671\mu m$. It is equipped with two direct detection cameras/medium resolution spectrometers, SPIRE (Spectral and Photometric Imaging Receiver) (Griffin et al. 2010) and PACS (Photodetector Array Camera and Spectrometer) (Poglitsch et al. 2010) and a very high-resolution heterodyne spectrometer, HIFI (Heterodyne Instrument for the Far-Infrared) (De Graauw et al. 2010).

SPIRE consists of an imaging photometer with three broad bands centred on 250μm, 350μm and 500μm and a two-band imaging Fourier-Transform spectrometer (FTS) covering 194 – 318μm and 294 – 671μm.

We extracted contours from the *Herschel* SPIRE 500 μm dust continuum emission map within a square box of side 35 arcmin around the center of the cluster NGC 1912. Subsequently, these contours were superimposed onto the cluster's extinction map for comparative analysis. The data has been obtained from the Herschel Science Archive

2.4 GALEX Data

The California Institute of Technology led the NASA mission called the Galaxy Evolution Explorer (*GALEX*), with its principal objective of investigating the evolution of galactic star formation. The mission involved spectroscopic and imaging surveys in two wavelength ranges: far ultra-violet (FUV : 1344 - 1786 Å) and near ultra-violet (NUV: 1771-2831 Å). With a spatial resolutions of 4.2″ and 5.3″, respectively in FUV and NUV and a wide FOV of ∼ 1.3°. *GALEX* conducted sky surveys of varying depth and coverage, including the All-sky imaging survey (AIS), Medium-depth imaging survey (MIS), Deep imaging sky survey (DIS), and Guest investigator (GII) survey (Morrissey et al. 2007; Bianchi 2009).

We have conducted a cross identification of the cluster members of NGC 1912 with their *GALEX* counterparts, to detect NUV sources, using the MAST (Barbara A. Mikulski Archive for Space Telescopes) Data Discovery portal.

3 CLUSTER MEMBERSHIP ANALYSIS

The stars belonging to the same cluster exhibit consistent center-of-mass motion and are located at the same distance. Consequently, cluster membership analysis based on the highly precise parallax and proper motion data in *Gaia* DR3, offer reliable results. It is important to be noted that evaluating the membership for more distant clusters becomes challenging, mainly due to the limitations in the precision of parallax data.

In the present study, we have used the technique proposed by Deb et al. (2022) (Hereafter, SD22) to estimate the membership of stars in the open cluster NGC 1912. It is an improved ensemble based unsupervised machine learning method for cluster membership determination. The method uses a combination of k-Nearest Neighbour (kNN) (Cover & Hart 1967), Mahalanobis Distance (MD) (Mahalanobis 1936) and Gaussian mixture modelling (GMM) (McLachlan & Peel 2000) for the membership determination. In SD22 the authors have discussed certain advantages of their method in comparison to some of the earlier methods (e.g., Gao 2018; Agarwal et al. 2021). Furthermore, the difficulties encountered in Dias et al. (2014) for the membership determination of some of the clusters could also be overcome following the approach in SD22. As noted by the authors in Dias et al. (2014), their technique might not provide satisfactory results when there is an overlap between the cluster and field stars in the proper motion space.

The SD22 method operates without the need for any pre-existing knowledge about the cluster, unlike some methods in the literature e.g., Cantat-Gaudin et al. (2018) (Hereafter CG18). CG18 requires a priori information (distance and radius) for the membership analysis (Agarwal et al. 2021). The SD22 method facilitates the direct utilization of three-dimensional Gaia data (π, $\mu_\alpha \cos\delta$, μ_δ) for MD calculation, eliminating the need for preprocessing steps. Whereas, the methods like HDBSCAN (Hunt & Reffert 2021, 2023) require some preprocessing on the data, prior to the membership analysis. However, the SD22 method is not suitable for identifying new, undiscovered clusters based on over-densities in multidimensional data, due to its potential computational expense.

The following sections discuss the detailed methodology applied for the membership analysis of NGC 1912 in two stages.

3.1 Stage 1: Outlier removal by k-Nearest Neighbour (kNN)

The primary objective of this step is to make an initial approximation of range of the target cluster parameters (π, $\mu_\alpha \cos\delta$ and μ_δ). This is achieved by applying the k-Nearest Neighbour (kNN) technique to a region where the number of cluster stars is significantly greater than that of the field stars. For this step, we downloaded the data for NGC 1912 from the *Gaia* DR3 database within a 10′ search radius (with the constraint of $\pi \geq 0$). This provided us with 3660 stars. A small search radius is used to ensure the dominance by cluster stars rather than field stars. Furthermore, a bigger search radius might inadvertently include a nearby cluster (if any), thereby compromising the accuracy of our parameter range estimation (Deb et al. 2022).

The kNN method identifies a data point as an outlier based on its distance from the local neighborhood. For a data point x, its mean nearest neighbor distance from k numbers of its nearest neighbors is denoted as $\bar{d}_{NN}$ and expressed as follows (Deb et al. 2022).

$$\bar{d}_{NN} = \frac{\Sigma_k d(x,k)}{NN_k} \quad (1)$$

Here, $d(x,k)$ represents the Euclidean distance between a data point x and its k closest neighbors within a 3D space defined by π,

---

[1] "Herschel is an ESA space observatory (Pilbratt, G. L. et al. 2010) with science instruments provided by European-led Principal Investigator consortia and with important participation from NASA"

Table 1. The parameter ranges for π, $\mu_\alpha cos\,\delta$ and μ_δ for NGC 1912 obtained from Stage 1 (kNN)

Cluster	Radius ($''$)	Cut-off $\overline{d}_{\rm NN}$	π mas	$\mu_\alpha cos\,\delta$ mas yr^{-1}	μ_δ mas yr^{-1}
NGC 1912	10	0.03	[0.8, 0.95]	[1.2, 1.8]	[-5, -4]

$\mu_\alpha cos\delta$, and μ_δ. For this study we considered the number of nearest neighbour (k) = 5. The term NN_k denotes the total number of nearest neighbors. It is well understood that for a star which is a member of the target cluster, the $\overline{d}_{NN}$ value should be smaller as compared to that of a field star. Accordingly, we selected a threshold value (t) = 0.03 for $\overline{d}_{NN}$ beyond which we have classified a star as an outlier. There is no specific rule regarding the selection of the t value except the one that it has to be based on a smaller value of $\overline{d}_{NN}$ so as to retain a significant number of cluster stars (Deb et al. 2022). Fig. (1a) shows the distribution of $\overline{d}_{NN}$ for all the stars obtained within 10 $'$ search radius of NGC 1912 along with the selected t value. After the rejection of numerous outliers based on the chosen t value, 308 stars were retained. Fig. (1b) and (1c) shows these 308 stars overplotted on the proper motion (PMD) and the color-magnitude diagram (CMD) of all the stars obtained within 10 $'$ search radius of NGC 1912, respectively. Histograms illustrating the distribution of these 308 stars in the spaces of π, $\mu_\alpha \cos\delta$, and μ_δ are presented in Fig. (1d), (1e), (1f). We thus obtained the range of parameters as: 0.8 < π < 0.95 mas, 1.2 < $\mu_\alpha \cos\delta$ < 1.8, and -5 < μ_δ -4. They are listed in Table 1.

3.2 Stage 2: Gaussian mixture model (GMM) on Mahalanobis Distance (MD) distribution

In this stage we use the range of cluster parameters obtained from stage 1 to eliminate a significant number of field stars from a bigger dataset of the target cluster in order to carry out the final membership analysis. A search within a 2° radius (considering stars with parallax ≥ 0) of NGC 1912 yielded a total of 362,847 stars. Subsequently, we filtered the dataset to include only those stars whose parameters (π, $\mu_\alpha \cos\delta$, μ_δ) were within the range obtained in the stage 1. This resulted in a refined dataset containing 1034 stars. Following this, MD calculations were performed for each star in the three-dimensional parameter space. The MD of an observation $\vec{x} = (x_1, x_2, ..., x_n)$ within a dataset having a mean $\vec{\mu} = (\mu_1, \mu_2, ..., \mu_n)$ and covariance matrix Σ is defined as (Mahalanobis 1936)

$$D_M(\vec{x}) = \sqrt{(x-\mu)^T \Sigma^{-1} (x-\mu)} \tag{2}$$

A Gausian Mixture Model (GMM) is used to effectively reproduce a data distribution using a finite number of Gaussian distributions (McLachlan & Peel 2000; Deisenroth et al. 2020). We modelled the MD distribution obtained for 1034 stars using two Gaussian distributions: one representing cluster stars and the other field stars. The membership probability, or responsibility, indicating the likelihood that a star with MD ($D_{M,i}$) belongs to a class k = {c, f}, where "c" denotes "cluster" and "f" denotes "field", is expressed as (Deisenroth et al. 2020)

$$r_{ik} = \frac{\omega_k P_k(D_{M,i}|\mu_k, \sigma_k^2)}{\Sigma_k \omega_k P_k(D_{M,i}|\mu_k, \sigma_k^2)} \tag{3}$$

where, $P_k(D_M|\mu_k, \sigma_k^2)$ denotes the Gaussian probability distributions and ω_k, μ_k and σ_k^2 represent the weight, mean, and variance, respectively. The parameters $(\omega_k, \mu_k, \sigma_k^2)$ were determined through the expectation-maximization (EM) algorithm (Deb et al. 2022) wherein we begin with some initial guess and subsequently, calculate the responsibilities for each class using Equation 3, employing the current parameter values (E-step). The parameters are then re-estimated using the current responsibilities from the E-step (M-step). This steps are repeated until convergence. Using the final parameter values, we calculate the membership probabilities of all the stars towards the cluster ‘c’ as

$$r_{ic} = \frac{\omega_c P_c(D_{M,i}|\mu_c, \sigma_c^2)}{\Sigma_k \omega_k P_k(D_{M,i}|\mu_k, \sigma_k^2)}$$

Considering a membership probability value > 0.50, we identified 401 cluster members for NGC 1912. We fit a Gaussian to the parallax and proper motion distributions of these stars and obtain the mean values as $\overline{\pi}$ = 0.877 ± 0.001 mas, $\overline{\mu_\alpha cos\delta}$ = 1.533 ± 0.004 mas yr^{-1} and $\overline{\mu_\delta}$ = -4.434 ± 0.005mas yr^{-1}. The errors have been calculated using the formula $\sigma/\sqrt{N}$, where σ is the standard deviation of the sample and N denotes the sample size. The mean values of these parameters reported in CG18 are π = 0.874 ± 0.003 mas, $\mu_\alpha cos\delta$ = 1.580 ± 0.009 mas yr^{-1} and μ_δ = -4.424 ± 0.008 mas yr^{-1}. Our findings demonstrate a remarkable concordance with these results within the specified error limits. CG18 carried out the membership analysis considering sources with G < 18 mag from *Gaia* DR2 (Gaia Collaboration et al. 2018). They used the clustering algorithm UPMASK (Krone-Martins & Moitinho 2014). Even though our analysis was based on a fainter magnitude limit of G < 21, the number of member stars reported by CG18 is slightly higher than us. This difference might be due to the fact that CG18 performed a broad selection of parallax values i.e., within 0.5 mas of the value obtained from the literature. Whereas, in our analysis, we imposed a more stringent bound, permitting a narrower range of parallax values with the constraint : parallax ∈ [0.8, 0.95] mas (as listed in Table 1). Fig. (2a) visualizes the proper motions for the 401 cluster members, while Figure (2b) shows the CMD of these stars. The color-coding in these figures corresponds to their membership probability. The clean CMD of all the member stars obtained for NGC 1912 suggests a reliable membership analysis.

Fig. (3) presents the CMD of the member stars (gray circles) of NGC 1912 with the following data overlays : (i) 67 *GALEX* counterparts in NUV band (magenta squares); (ii) *Gaia* counterparts of 90 stars towards NGC 1912 (black circles), that have been subjected to polarimetric analysis (listed in Table 3), including 21 identified members among them (green triangles); (iii) 3 Be stars (teal pentagon), 1 blue straggler (BS; pink star), and 4 red giants (RG; filled brown plus), identified by Høg et al. (2000) (all of these 8 stars are located within or in close proximity to the region selected for polarimetric observation in this work); (iv) 24 variable stars observed by Li et al. (2021), including 8 Gamma Doradus (γ Dor; blue plus), 8 Delta Scuti (δ Scuti; red plus) and 7 eclipsing binaries including 4 W UMa (EW; black plus) and 3 Algol (EA; green plus) type variables and 1 variable star of unknown type (cyan plus) (14 of these variable stars including the 3 γ Dor, 5 δ Scuti, 3 EW, 2 EA and the unknown type variable are also positioned within or near the polarimetrically observed region). It is evident from Fig. (3) that the majority of the NUV sources are located towards the high-mass region on the CMD. Table A1 lists the *Gaia* ID (Identification numbers from the original works have been given in parentheses), G magnitude, $G_{BP} - G_{RP}$ colour and the membership probability according to CG18 and this work for a total of 32 stars (including the 24 variable stars from Li

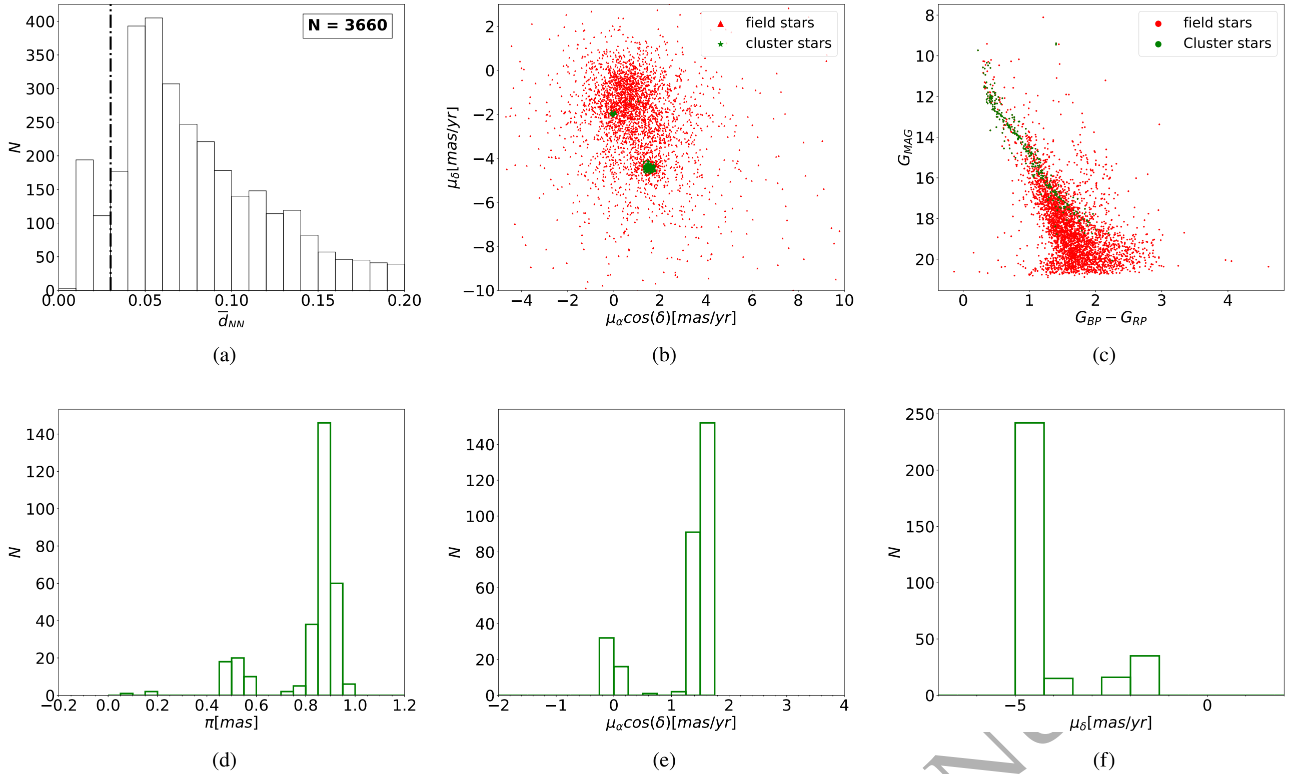

(a) (b) (c)

(d) (e) (f)

Figure 1. (a): $\overline{d}_{NN}$ distribution for 3660 stars found within 10-arcmin search radius of NGC 1912. The black dashed line indicates the threshold value (t) = 0.03. (b): The proper motion distribution and (c): Color-Magnitude diagram, for the 308 stars (in green) selected using $\overline{d}_{NN}$ < 0.03, overlaid on 3660 stars (in red) found within 10-arcmin of NGC 1912. Histogram plots of (d): π, (e): $\mu_\alpha \cos\delta$ and (f): μ_δ for the 308 selected stars.

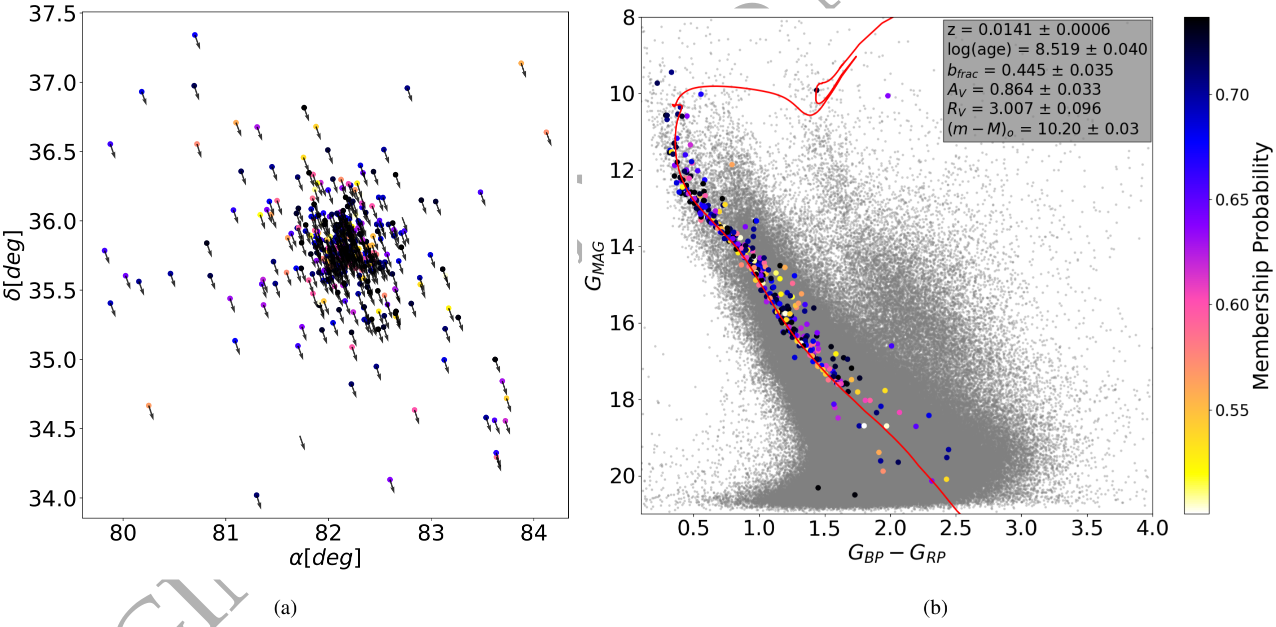

(a) (b)

Figure 2. (a): Vector plot illustrating the proper motion of the 401 member stars of NGC 1912 at their sky-positions. (b): CMD of the 401 member stars found within 2° of NGC 1912 overplotted on the field stars (in gray). The red curve represents the best-fit theoretical isochrone obtained using ASteCA. The optimal parameter values are presented in the box on the top right corner

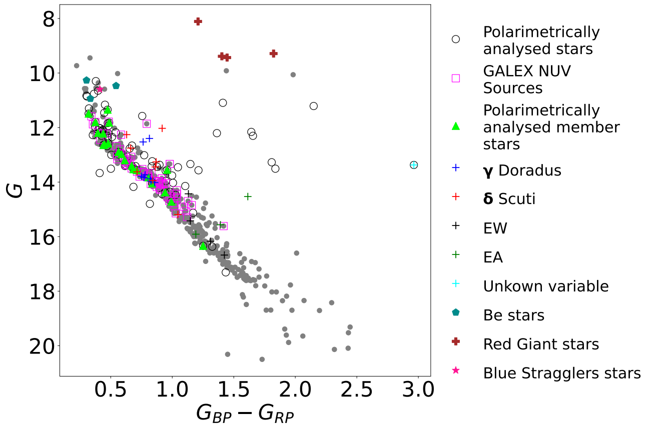

Figure 3. CMD showing the members of NGC 1912 in gray color along with their NUV counterparts from GALEX, the stars subjected to polarimetric analysis and additional stars identified by previous works.

et al. (2021) and the additional 8 stars i.e, 3 Be, 1 blue straggler and 4 red giants, from Høg et al. (2000)). While CG18 identifies 6 members among the 24 variable stars, our technique recognizes only two members, listed with serial numbers #5 and #14 in Table A1. The blue straggler star (star number #32 according to Table A1) is recognized as a member by both our analysis and CG18. Membership probabilities of some stars are missing as they were already excluded as outliers by the stage 1 of the membership analysis.

3.3 Cluster Parameters

Cluster study remains incomplete without determining the fundamental cluster parameters (distance, metallicity, age, extinction or reddening, binary fraction, total-to-selective extinction ratio). This can be obtained by fitting the theoretical isochrones available in the literature (e.g., Bressan et al. 2012; Marigo et al. 2017; Girardi et al. 2002) to the colour-magnitude diagrams (CMD) (e.g, Monteiro, H. et al. 2010; Dias et al. 2012; Perren, G. I. et al. 2015; Singh et al. 2020) of the cluster. For this purpose, we used the Automated Stellar Cluster Analysis (ASteCA) package developed by Perren, G. I. et al. (2015). The newer version, ASteCA v 0.4.3 (Perren et al. 2022) samples the distributions of fundamental parameters using the ptemcee parallel tempering Bayesian inference method. We used the theoretical isochrones PARSECv1.2s (Bressan et al. 2012; Tang et al. 2014; Chen et al. 2015) (for Gaia EDR3 passbands) from CMDv3.7 web service along with the *Gaia* DR3 photometric data of the members of NGC 1912, as an input to ASteCA. The best-fitted isochrone obtained is shown in Figure 2b. The best-fit values that were obtained are Metallicity (z)[2] = 0.0141 ± 0.0006, log(age) = 8.519 ± 0.040 (≈ 330 ± 30 Myr), binary fraction (b_{frac}) = 0.445 ± 0.035, visual extinction (A_V) = 0.864 ± 0.033 mag, total-to-selective extinction ratio (R_V) = 3.007 ± 0.096 and distance modulus ($(m-M)_\circ$) = 10.20 ± 0.03 mag, respectively. From the relation, $E(B-V) = A_V/R_V$, the reddening $E(B-V)$ is found as ~ 0.29 ± 0.02 mag. Distance modulus value provided by ASteCA is already corrected for extinction. Hence, the distance to the cluster can be calculated as 1096 ± 15 pc.

Dias et al. (2021) used *Gaia* DR2 data with an updated isochrone fitting code from Monteiro et al. (2020) to report the cluster parameters for NGC 1912 as : $[Fe/H] = 0.014 \pm 0.082$, Distance = 1068 ± 26 pc, log(age) = 8.412 ± 0.112, A_V = 1.006 ± 0.063 mag, for NGC 1912. Binary fraction for NGC 1912 was reported by Almeida et al. (2023) (using *Gaia* EDR3 data) as ≃ 0.44. Our estimates are close to these literature values. The estimated reddening is also consistent with that obtained from *UBV* photometry in Johnson et al. (1961).

3.4 Radial Density Profile

The radial surface density profile of an open cluster is given as King (1962).

$$\rho(r) = \rho_o \left(\frac{1}{\sqrt{1+\left(\frac{r}{r_c}\right)^2}} - \frac{1}{\sqrt{1+\left(\frac{r_t}{r_c}\right)^2}} \right)^2 + \rho_{bg} \tag{4}$$

where, ρ_o = central density, ρ_{bg} = background density, r_c = core radius, r_t = tidal radius of the cluster.

We computed the radial distance (r) of the i^{th} cluster member (α_i, δ_i) from the center of the cluster (α_o, δ_o) as

$$\cos(r) = \cos\delta_i \cos\delta_o \cos(\alpha_i - \alpha_o) + \sin\delta_i \sin\delta_o \tag{5}$$

where, i ranges from 1 to N, where N represents the number of cluster members. The stellar surface density is computed as $\rho_i = N_i/A_i$, where N_i = number of stars in the i^{th} ring with inner and outer radii r_i and r_{i+1}, respectively and $A_i = \pi r_{i+1}^2$ - πr_i^2. Assuming Poisson statistics, we determined the uncertainty in density as $\sigma_{\rho_i} = \sqrt{N_i/A_i}$.

We applied the Bayesian MCMC technique to fit the radial density profile to the true cluster members and determine the parameter values and uncertainties. We used the package EMCEE (Foreman-Mackey et al. 2013) for this purpose. We configured our program with 100 walkers, 50000 iterations, and 500 burn-in steps. Fig. (5) shows the marginalized posterior distributions for all the parameters in Eq. 4. The distribution mean (50th percentile) is taken as the best-fit value of the parameters. The negative and positive statistical uncertainties are based on the 16th and 84th percentiles, respectively. The black lines on each histogram depict the mean, while the magenta dotted lines indicate the uncertainties. Fig. (4) shows the best-fitting line (red) to the observed data (black dots). The blue lines represent the 300 random sample fits from the MCMC chains. The optimal parameter values obtained for the cluster NGC 1912 are ρ_o = 0.643 ± 0.067 stars arcmin^{-2}, r_c = 7.743 ± 0.784 arcmin (≈ 2.47 ± 0.28 pc), r_t = 84.633 ± 7.188 arcmin (≈ 26.98 ± 2.66 pc), and ρ_{bg} = 0.001 ± 0.000 stars arcmin^{-2}.

Our estimates for r_c and r_t closely align with those obtained by Tarricq, Y. et al. (2022). They similarly used the King (1962) function to fit the observed radial density profile of the cluster. Furthermore, our derived r_c value corresponds well with the findings of Cordoni et al. (2023). However, the central density value estimated by Cordoni et al. (2023) is ≈ 1.037 arcmin^{-2} higher than our own estimate. Notably, Cordoni et al. (2023) employed the EEF function (Elson et al. 1987) for least square fitting of the observed density profile of the cluster.

3.5 Mass Segregation

To investigate the mass segregation effect in the cluster NGC 1912, we plot a G-R diagram for the member stars, where G and R represents the *G* band magnitude and the distance to the cluster center,

---

[2] The metallicity in z corresponds to $[Fe/H] = \log(z/z_\odot)$ (Perren, G. I. et al. 2015), where $z_\odot = 0.0152$ Bressan et al. (2012)

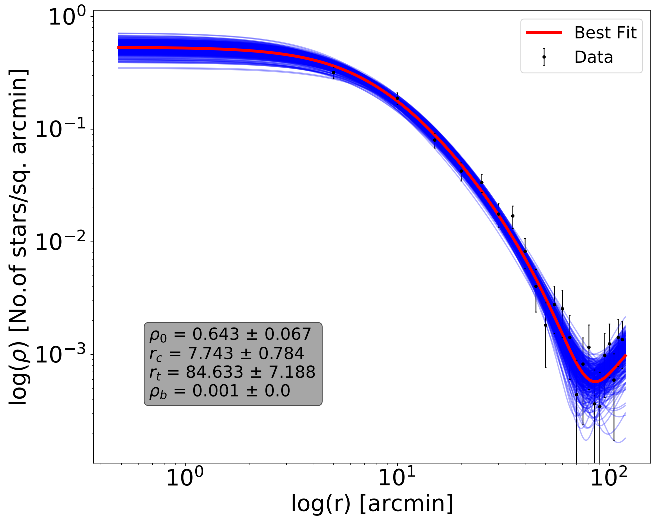

Figure 4. King profile fit for all the members stars of NGC 1912. The error bars are equivalent to the 1σ Poissonian uncertainties. 300 random sample fits from the MCMC chains are represented by blue lines.

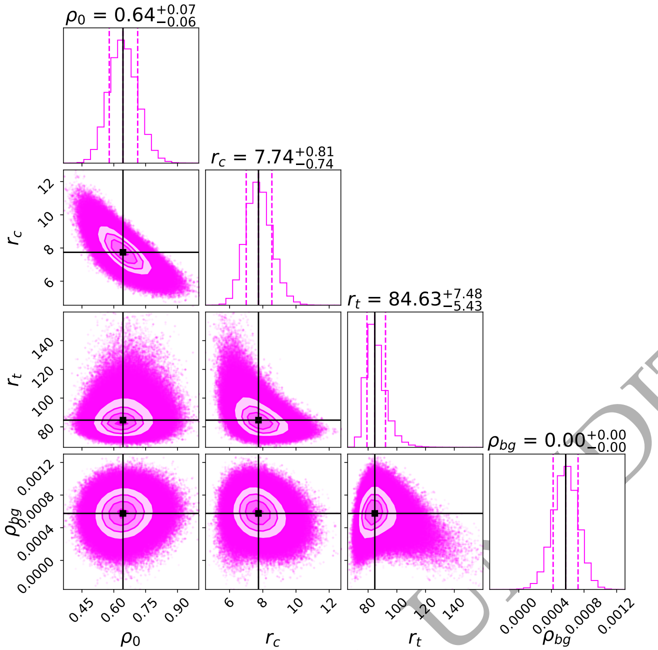

Figure 5. Marginalized posterior distribution and uncertainties of model parameters for the King profile fit to the members of NGC 1912. The parameter values correspond to the sample mean (50th percentile) and 16th (down) and 84th (up) percentile differences. The black vertical lines on each histogram correspond to the 50th percentile and magenta dotted lines represent 16th and 84th percentiles, respectively. Corner package (Foreman-Mackey et al. 2013) was used for the generation of this plot

respectively, as shown in the Fig. (6a). It can be clearly seen that the brighter (massive) stars lie more towards the center and the fainter (lighter) stars lie farther away from the center. Similar results for NGC 1912 has also been found by Pandey et al. (2007) and Almeida et al. (2023)[3]. The data points enclosed by magenta circles correspond to GALEX-NUV sources. It is seen that a majority of these NUV sources exhibit high mass and are concentrated more towards the center. Fig. (6b) shows the radial cumulative distribution function (CDF) for the members stars of NGC 1912 in three magnitude bins ($G \leq 13.4$, $13.4 < G \leq 15.8$ and $G > 15.8$). The x-axis represents radial distances (r) for member stars, while the y-axis indicates the probability that a randomly chosen star falls at or below a given radial distance. Analysis of Figure (6b) reveals some distinctive trends: up to $r \approx 17$ arcmin, the CDFs of intermediate ($13.4 < G \leq 15.8$) and low-mass ($G > 15.8$) stars show similar trends, both significantly lower than that of high-mass ($G \leq 13.4$) stars. This observation suggests a higher concentration of massive stars closer to the cluster center. Beyond $r \approx 17$ arcmin, the CDF of intermediate-mass stars begin to rise relative to that of low-mass stars. Notably, around $r \approx 95$ arcmin, the CDF of low-mass stars seems to exhibit a rise, indicating an increased probability of encountering such stars towards the outer regions of the cluster. These findings strongly imply the presence of dynamical mass segregation within the NGC 1912 cluster.

4 POLARIMETRIC ANALYSIS

The polarimetric observation for NGC 1912 was carried out in four fields centered at R.A. : 5h28m33.1s, Dec : +35°54m50.4s; R.A. : 5h28m18.9s, Dec : +35°45m39.6s; R.A. : 5h28m59.2s, Dec : +35°51m18s and R.A. : 5h28m43.4s, Dec : +35°42m14.4s (shown in Fig. (7); details regarding this figure has been discussed later in this section), in B, V, R_c and I_c photometric filters, reaching down to a limiting magnitude of V $\simeq$ 18 mag, on 23rd and 24th december 2011, using the ARIES IMaging POLarimeter (AIMPOL; Rautela et al. 2004), mounted on the back-end of the $104-cm$ Sampurnanand f/13 Cassegrain Telescope of ARIES, Nainital. AIMPOL produces ordinary and extraordinary images of its field of view (FOV) in slightly different directions separated by ~ 27 pixels. To achieve this a half-wave plate (HWP) modulator and a beam-splitting Wollaston prism analyser are integrated into the telescope beam path. We carried out the imaging using a TK 1024x1024 pixel^2 charged-coupled device (CCD) which has a FOV $\sim 8'$ diameter on the sky. Each CCD pixel corresponds to $1.73''$. In order to project the telescope focal plane on the CCD surface, a focal reducer (85mm, f/1.8; with a reduction factor of ~ 4.7) is placed between Wollaston prism and CCD camera . The gain and read out noise of the CCD are 11.98 e^-/ADU and 7.0 e^-, respectively (Medhi et al. 2007, 2008, 2010; Singh et al. 2020).

Standard aperture photometry following bias subtraction was conducted to determine the flux of the ordinary (I_o) and extraordinary image (I_e) of the target stars using Image Reduction and Analysis facility (IRAF)[4]. The full width at half-maximum (FWHM) of the stellar images vary from 2 to 3 pixel. Theoretically, the intensities of ordinary and extra-ordinary beams after emerging out of the Wollaston prism are given by

$$I_e(\alpha) = \frac{I_{up}}{2} + I_p Cos^2(\theta - 2\alpha) \tag{6}$$

---

[3] Detailed plots in relation to the study of mass segregation of NGC 1912 and other clusters from the work of Almeida et al. (2023) are available at `https://ocmass.streamlit.app/Detailed_MF`

[4] "IRAF is distributed by National Optical Astronomical Observatories, USA"

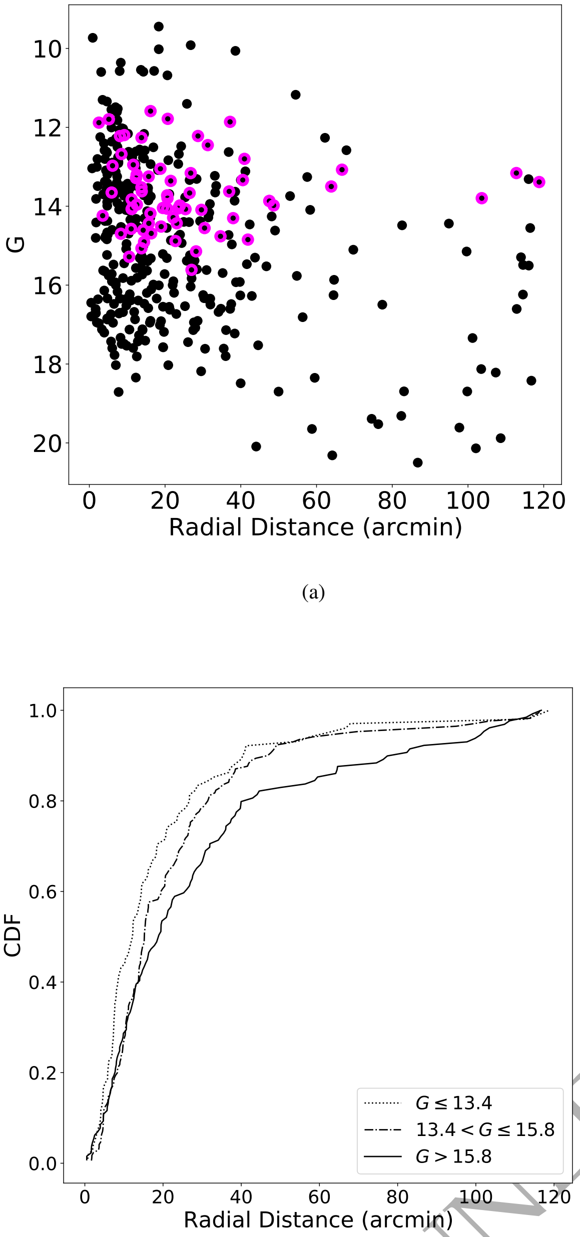

(a)

(b)

Figure 6. (a): Plot of G magnitude against radial distance for the members of cluster NGC 1912. Points enclosed by magenta circles correspond to GALEX-NUV sources. (b): Plot of the radial cumulative distribution function for the members stars of NGC 1912 in three magnitude bins ($G \leq 13.4$, $13.4 < G \leq 15.8$ and $G > 15.8$)

$$I_o(\alpha) = \frac{I_{up}}{2} + I_p Sin^2(\theta - 2\alpha) \tag{7}$$

Here, I_{up} and I_p represent the unpolarized and polarized intensities of the incoming beam, respectively. θ and α denote the position angles (with reference to the axis of the Wollaston prism, which is aligned along the celestial the North-South direction) of the polarization vector and the half-wave plate fast-axis, respectively Ramaprakash, A. N. et al. (1998). From the Eq. 6 and 7, a ratio $R(\alpha)$ is defined as

$$R(\alpha) = \frac{\frac{I_e(\alpha)}{I_o(\alpha)} - 1}{\frac{I_e(\alpha)}{I_o(\alpha)} + 1} = PCos(2\theta - 4\alpha) \tag{8}$$

where $P = \frac{I_p}{I_p + I_{up}}$ represents the fraction of the total light which shows linear polarization. The ratio $R(\alpha)$ corresponds to the normalized Stokes' parameter q ($= Q/I$; where I $= I_p + I_{up}$ represents the total intensity) for $\alpha = 0°$ (HWP fast axis is aligned to the reference axis). Similarly, the normalized Stokes' parameter u ($= U/I$), q_1 ($= Q_1/I$), u_1 ($= U_1/I$) are also the ratios $R(\alpha)$, for $\alpha = 22.5°$, $45°$ and $67.5°$, respectively.

In theory, the determination of the degree of polarization (P) and position angle of polarization (θ) can rely solely on two Stokes' parameters, q and u. However, pragmatic scenarios tend to be more complex (Medhi et al. 2007, 2008, 2010). As a result, the signals measured in the two images (I'_e and I'_o) may deviate from the actual values (I_e and I_o) (Ramaprakash, A. N. et al. 1998). Thus Eq. 8 can be rewritten as

$$R(\alpha) = \frac{\frac{I'_e(\alpha)}{I'_o(\alpha)} \times \frac{F_o}{F_e} - 1}{\frac{I'_e(\alpha)}{I'_o(\alpha)} \times \frac{F_o}{F_e} + 1} = PCos(2\theta - 4\alpha) \tag{9}$$

where F_o and F_e account for the practical considerations and the ratio is given by

$$\frac{F_o}{F_e} = \left[\frac{I'_o(0°)}{I'_e(45°)} \times \frac{I'_o(45°)}{I'_e(0°)} \times \frac{I'_o(22.5°)}{I'_e(67.5°)} \times \frac{I'_o(67.5°)}{I'_e(22.5°)} \right]^{\frac{1}{4}} \tag{10}$$

Hence, we require two additional measurements at $\alpha = 45°$ and $\alpha = 67.5°$ (normalized Stokes' parameters u_1 and q_1). In order to make a uniform response, we used Eq. 9, instead of the robust flat fielding technique. The values of P and θ along with their associated errors (e_P and e_θ) were obtained by fitting the cosine curve to the four values of R(α). The errors associated with $R(\alpha)$ is given by

$$\sigma_{R(\alpha)} = \frac{\sqrt{I_e + I_o + 2I_b}}{I_e + I_o} \tag{11}$$

where I_b denotes the average background count around the ordinary and extraordinary image of the star. These errors associated with four values of $R(\alpha)$ were used as weights during the cosine fitting.

Three polarized and two unpolarized standard star (Schmidt et al. 1992) were also observed to check the calibration of the position angle and to determine the instrumental polarization, respectively. The observed degree of polarization (P) and position angle (θ) for the polarized standard stars (listed in Table 2) are found to be in agreement with the published values within the error limit. Stokes parameters q (per cent) and u (per cent) for the unpolarized standard stars are also shown in Table 2. We found the average instrumental polarization to be less than 0.4 per cent (Medhi et al. 2007, 2008, 2010; Singh et al. 2020). AIMPOL does not have a grid to avoid the overlapping of an ordinary image with the adjacent extraordinary image, hence, we exclusively considered isolated stars that exhibited no overlap between the ordinary and adjacent extraordinary images. Furthermore, we have selected only those stars for which $P/e_P > 3$. As a result, we reported the polarization measurements for a total of only 90 stars within the observed field of view of the NGC 1912

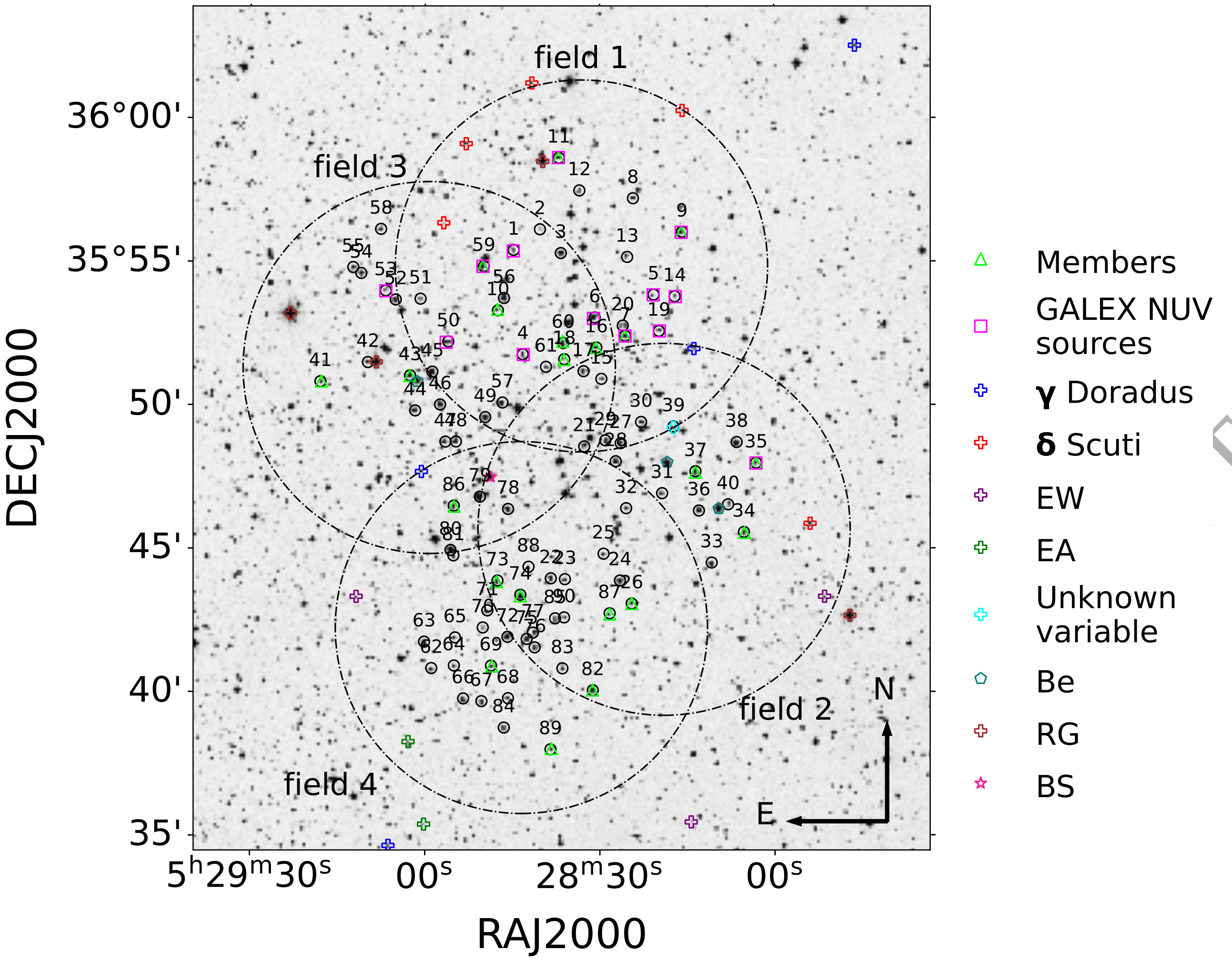

Figure 7. A 30′ × 30′ DSS R band image of the field containing NGC 1912. The North (N) and East (E) directions are indicated in the right hand bottom corner of the figure. The larger circles indicate the observed fields, with 90 stars (including 21 cluster members marked by green triangles) subjected to polarimetric analysis (smaller black circles), and corresponding IDs listed in Table 3. Additionally, the image highlights 13 GALEX-NUV sources coinciding with the analyzed stars, along with other stars situated within or near the polarimetrically observed region. These include 3 γ Dor, 5 δ Scuti, 3 EW, 2 EA type variables, 1 variable star of unknown type, 3 Be stars, 4 red giants, and 1 blue straggler.

cluster. We conducted astrometry on these observed sources using the CCMAP and CCTRAN packages in IRAF.

Table 3 lists, the 90 observed stars in the direction of NGC 1912, including their sky co-ordinates, the percentage of polarization, the position angle (in the equatorial coordinate system) and their respective errors for each filters. The range of percentage of polarization for the 90 stars as obtained in different filters are : P_B = 0.75 - 8.0 percent; P_V = 0.94 - 5.87 percent; P_R = 1.03 - 6.36 percent; P_I = 0.9 - 5.55 percent. The corresponding range of position angle obtained are : θ_B = 110.69° - 180.10°; θ_V = 129.72° - 165.36°; θ_R = 123.52° - 168.83°; θ_I = 133.74° - 182.44°. Fig. (9a) and (9b) shows the histogram of degree of polarization (in per cent) and position angle of polarization (in degree), respectively. It is to be noted that position angles (θ) greater than 180° is reported as $(\theta - 180)°$ in Table 3. For the observed stars, the sky projection of polarization vectors in the V band is shown in Figure 8, superimposed on the DSS R-band image of the NGC 1912 cluster. The observed stars are marked with black circles and the polarization vectors are drawn with black lines keeping the stars at the center. The length of each polarization vector is proportional to the percentage of polarization of the star. The inclination of the polarization vectors with respect to the north-south direction indicates the position angle of polarization. A reference line indicating a magnitude of 1 percent polarization is provided at the bottom left of Figure 8. The dashed black line signifies the orientation of the projection of the Galactic plane (GP) at b = 0.68°. The polarization vectors were observed to align almost parallel to the direction of the GP, with some small deviations. Considering all the 90 polarimetrically analyzed stars, the weighted average (using inverse squares of the respective errors as weighting factors) of polarization ($\overline{P}_V$) and position angle ($\overline{\theta}_V$) in V-filter are 2.13 ± 0.09 percent and 141.06° ± 1.09°, respectively. For other filters the values are $\overline{P}_B$ = 7.55 ± 0.57 percent, $\overline{\theta}_B$ = 154.92° ± 1.97°; $\overline{P}_R$ = 1.94 ± 0.10 percent, $\overline{\theta}_R$ = 149.24° ± 1.02°; $\overline{P}_I$ = 1.58 ± 0.11 percent, $\overline{\theta}_I$ = 149.27° ± 1.83°. When considering only member stars, the weighted average values are : $(\overline{P}_B)_m$ = 2.29 ± 0.17 percent, $(\overline{\theta}_B)_m$ = 151.23° ± 1.46°;$(\overline{P}_V)_m$ = 1.53 ± 0.21 percent, $(\overline{\theta}_V)_m$ = 154.15° ± 1.43°; $(\overline{P}_R)_m$ = 1.90 ± 0.15 percent, $(\overline{\theta}_R)_m$ = 149.32° ± 2.11°; $(\overline{P}_I)_m$ = 1.70 ± 0.19 percent, $(\overline{\theta}_I)_m$ = 147.65° ± 7.16°. For non-member stars, the weighted average values are : $(\overline{P}_B)_{nm}$ = 7.8 ± 0.67 percent, $(\overline{\theta}_B)_{nm}$ = 154.94° ± 2.54°;$(\overline{P}_V)_{nm}$ = 2.35 ± 0.11 percent, $(\overline{\theta}_V)_{nm}$ = 140.23° ± 1.32°;

Table 2. Polarization and Position Angles of Polarized standard and Stokes' parameters for unpolarized standard stars

Present Work			Schmidt et al. (1992)	
		Polarized Standard Stars		
		BD +59°389	(R.A. : 02 02 04.88; Dec : +60 15 26.5)	
Passband	$P \pm e_p$ (per cent)	$\theta \pm e_\theta (^\circ)$	$P \pm e_p$(per cent)	$\theta \pm e_\theta (^\circ)$
B	6.22 ± 0.11	99.09 ± 0.51	6.35 ± 0.04	98.14 ± 0.16
V	6.85 ± 0.05	98.43 ± 0.22	6.70 ± 0.02	98.09 ± 0.07
R_c	6.35 ± 0.01	97.67 ± 0.02	6.43 ± 0.02	98.14 ± 0.10
I_c	6.03 ± 0.13	98.04 ± 0.60	5.80 ± 0.02	98.23 ± 0.11
		HD19820	(R.A. : 03 12 05.35; Dec : +59 33 47.7)	
B	4.54 ± 0.03	114.75 ± 0.19	4.67 ± 0.04	115.70 ± 0.16
V	4.70 ± 0.03	114.59 ± 0.18	4.79 ± 0.03	114.93 ± 0.16
R_c	4.65 ± 0.05	114.93 ± 0.29	4.53 ± 0.03	114.46 ± 0.16
I_c	4.29 ± 0.03	114.67 ± 0.18	4.08 ± 0.02	114.48 ± 0.17
		Hiltner 960	(R.A. : 20 23 28.60; Dec :+39 20 57.00)	
B	5.62 ± 0.20	54.65 ± 1.04	5.72 ± 0.06	55.06 ± 0.31
V	5.70 ± 0.14	53.37 ± 0.08	5.66 ± 0.02	54.79 ± 0.11
R_c	5.20 ± 0.06	54.80 ± 0.30	5.21 ± 0.03	54.54 ± 0.16
		Unpolarized Standard stars		
Passband	q (per cent)		u (per cent)	
		HD21447	(R.A. : 03 30 00.21; Dec : +55 27 07.0)	
B	0.019		0.011	
V	0.037		-0.031	
R_c	-0.035		-0.039	
		HD14069	(R.A. : 02 16 45.16; Dec : +07 41 11.1)	
B	0.038		-0.010	
V	0.021		0.018	
R_c	0.010		-0.014	

$(\overline{P}_R)_{nm}$ = 1.94 ± 0.12 percent, $(\overline{\theta}_R)_{nm}$ = 149.23° ± 1.16°; $(\overline{P}_I)_{nm}$ = 1.47 ± 0.14 percent, $(\overline{\theta}_I)_{nm}$ = 150.99° ± 0.97°. The position angle of the GP (θ_{GP}) with respect to the North-South direction is 146.42°. The mean value of polarization position angle $\langle\theta\rangle$ represents the orientation of the envelope magnetic field (θ_B^{env}) in the region. The offset between the envelope magnetic field and the orientation of the GP, considering all the stars subjected to polarimetric analysis, is $\theta_{\text{off}} = |\theta_B^{env} - \theta_{GP}| \sim 8.5^\circ, 5.35^\circ, 2.82^\circ$ and 2.85° in B, V, R_c and I_c passbands, respectively. For only the member stars among them $(\theta_{\text{off}})_m \sim 4.81^\circ(B)$, $7.73^\circ(V)$, $2.90^\circ(R_c)$ and $1.23^\circ(I_c)$. Considering only the non-member stars, $(\theta_{\text{off}})_{nm}$ is $\sim 8.52^\circ(B)$, $6.18^\circ(V)$, $2.81^\circ(R_c)$ and $4.57^\circ(I_c)$. It is to be noted that a considerable number of stars studied for polarization exhibit intrinsic polarization and/or rotation in polarization angle (discussed in detail in the section 5), which also has a contribution to the measured offset. Despite these factors, there appears to be a near alignment between the envelope and the galactic magnetic field. Therefore, it is reasonable to conclude that the galactic magnetic field exerts predominant influence in this region.

One of the stars (star no. #3) in Table 3 is common to star #S13 reported by Subramaniam & Sagar (1999) [see table 4 of Subramaniam & Sagar (1999)], where the authors reported the Spectral Classification of this star as A6 III. Fig. (7) shows a 30′ × 30′ DSS R band image of the field containing NGC 1912. The 4 fields of polarimetric observation are shown in the figure by large circles. Smaller black circles mark the 90 stars subjected to polarimetric analysis, with 21 of them, having membership probability > 0.5 and hence identified as members (membership probabilities listed in Table 4). The members are shown by green triangles. The figure also includes 13 GALEX-NUV sources coinciding with analyzed stars, along with the additional stars (already mentioned in section 3.2) that are situated within or in close proximity to the polarimetrically observed region. From the discussion in section 3.5, it becomes clear that the existence of NUV counterparts to the observed stars suggests the presence of some apparently massive stars within the region under polarimetric observation. Among the observed stars, the star located farthest from the cluster center has an angular distance (along the plane of the sky) of approximately 11.45 arcmin from the center (as it is also evident from Fig. 10). Therefore, all the observed stars lie close to the cluster center within the plane of the sky. It is important to emphasize that while they appear close to the cluster center in the plane of the sky, their line-of-sight distances may vary. Consequently, the observed region could include stars that are either in the foreground or background. Thus, in accordance with the concept of dynamical mass segregation, it again indicates that some of these stars may potentially possess higher masses. This argument is further supported by Fig. (3), where some of the polarimetrically analyzed stars are located towards the high-mass region of the CMD. Using the

Table 3. Observed BVR_cI_c polarization values for different stars in NGC 1912.

ID	RAJ2000 (°)	DECJ2000 (°)	$V_{\rm mag}$ mag	$P_{\rm B}$ percent	$e_{P_{\rm B}}$ percent	$\theta_{\rm B}$ (°)	e_{θ_B} (°)	P_V percent	$e_{P_{\rm V}}$ percent	$\theta_{\rm V}$ (°)	$e_{\theta_{\rm V}}$ (°)	$P_{\rm R}$ percent	$e_{P_{\rm R}}$ percent	$\theta_{\rm R}$ (°)	$e_{\theta_{\rm R}}$ (°)	$P_{\rm I}$ percent	$e_{P_{\rm I}}$ percent	$\theta_{\rm I}$ (°)	$e_{\theta_{\rm I}}$ (°)
1	82.18663	35.92331	14.20	2.04	0.15	159.70	2.14	1.63	0.31	158.83	5.48	2.30	0.36	164.47	4.42	2.76	0.17	147.05	1.80
2	82.16775	35.93531	16.05	2.40	0.32	153.48	3.82	1.09	0.12	153.28	3.21	2.99	0.49	158.00	4.75	2.12	0.13	142.71	1.78
3[a]	82.15279	35.92150	12.29	-	-	-	-	1.45	0.01	163.16	0.23	-	-	-	-	1.71	0.29	158.64	4.88
4	82.18000	35.86271	14.82	1.77	0.06	155.96	0.96	1.27	0.38	145.27	8.53	1.20	0.36	152.02	9.78	1.99	0.32	148.04	4.56
5	82.08642	35.89736	15.68	1.58	0.45	139.56	8.20	1.89	0.14	149.42	2.13	2.05	0.21	134.00	2.88	2.16	0.32	159.50	4.30
6	82.12850	35.88408	12.45	1.74	0.06	159.48	0.95	1.09	0.09	146.23	2.24	1.38	0.37	159.59	7.74	1.54	0.27	141.92	4.99
7[m]	82.10675	35.87344	12.97	1.89	0.10	158.22	1.57	2.40	0.20	155.76	2.36	1.61	0.36	140.55	6.52	1.63	0.25	153.66	4.43
8	82.10110	35.95332	14.80	1.92	0.64	158.50	9.52	1.52	0.15	148.79	2.76	1.76	0.01	141.87	0.14	2.16	0.03	145.77	0.34
9[m]	82.06600	35.93381	13.70	2.33	0.30	150.41	3.65	1.60	0.22	139.87	4.00	2.19	0.21	151.31	2.70	0.90	0.08	134.60	2.46
10[m]	82.19788	35.88822	14.76	1.35	0.34	155.28	7.31	1.39	0.01	158.13	0.24	1.45	0.26	149.66	5.22	-	-	-	-
11[m]	82.15421	35.97683	15.67	2.50	0.36	158.20	4.13	2.63	0.80	146.62	8.89	2.01	0.29	124.40	4.09	1.43	0.38	149.20	7.52
12	82.13952	35.95788	16.43	1.10	0.14	0.10	3.72	2.12	0.06	165.36	0.88	3.05	0.27	123.52	2.57	2.91	0.54	145.08	5.38
13	82.10529	35.91925	15.03	0.90	0.03	123.00	0.85	1.71	0.10	129.72	1.73	1.58	0.06	124.68	1.07	1.79	0.18	140.32	2.92
14	82.07125	35.89633	15.35	1.64	0.28	144.46	4.87	1.87	0.28	144.78	4.36	2.65	0.20	168.83	2.19	1.69	0.43	148.15	7.31
15	82.12379	35.84843	14.63	1.62	0.04	146.21	0.75	1.28	0.19	156.20	4.35	2.72	0.04	126.97	0.44	1.41	0.07	133.74	1.45
16[m]	82.12738	35.86664	14.72	1.44	0.36	157.17	7.26	2.20	0.15	148.22	1.97	1.97	0.59	144.37	8.35	1.40	0.16	146.69	3.20
17	82.13654	35.85289	13.17	1.71	0.20	163.64	3.39	1.40	0.04	150.73	0.73	1.61	0.17	149.87	3.24	1.88	0.10	141.12	1.57
18[m]	82.15033	35.85986	15.64	1.56	0.04	155.06	0.65	1.65	0.13	154.76	2.30	1.34	0.09	139.80	1.95	1.55	0.33	154.36	6.10
19	82.08254	35.87625	15.64	2.40	0.10	161.79	1.17	1.33	0.03	155.90	0.71	2.04	0.14	168.29	2.03	1.98	0.31	169.48	4.52
20	82.10846	35.87936	14.66	1.29	0.16	145.97	3.57	1.70	0.02	153.81	0.36	1.78	0.23	143.21	3.75	2.19	0.04	157.38	0.46
21	82.13608	35.80919	13.59	-	-	-	-	2.38	0.16	142.44	1.96	2.50	0.21	147.28	2.46	1.98	0.26	140.18	3.76
22	82.15998	35.73259	13.60	3.37	0.27	155.98	2.25	1.27	0.04	153.21	0.90	2.09	0.30	143.59	4.17	1.77	0.02	142.89	0.37
23	82.14992	35.73211	14.90	3.25	0.16	153.12	1.42	2.25	0.38	144.73	4.79	2.74	0.22	140.48	2.29	3.16	0.34	150.83	3.04
24	82.11057	35.73133	12.71	3.21	0.18	143.13	1.61	3.01	0.07	146.50	0.69	2.70	0.10	143.48	1.07	2.49	0.18	145.35	2.09
25	82.12228	35.74689	14.56	1.89	0.24	152.73	3.56	2.42	0.15	145.14	1.72	2.88	0.38	150.40	3.75	2.64	0.32	152.36	3.46
26[m]	82.10217	35.71794	14.39	2.22	0.11	163.41	1.47	2.55	0.25	150.01	2.85	1.84	0.05	162.82	0.76	3.08	0.45	146.41	4.22
27	82.10996	35.81108	13.29	2.80	0.23	144.42	2.36	2.89	0.41	139.38	4.00	2.94	0.16	148.77	1.60	2.24	0.21	147.88	2.71
28	82.11354	35.80058	13.12	2.43	0.09	155.28	1.12	2.57	0.08	149.60	0.84	3.04	0.05	158.03	0.44	1.99	0.1	135.77	1.46
29	82.12099	35.81272	13.22	2.74	0.80	143.57	8.37	3.08	0.47	140.94	4.34	2.90	0.15	153.98	1.46	2.10	0.08	151.00	1.08
30	82.09538	35.82339	14.66	2.61	0.20	140.78	2.25	2.52	0.53	148.86	6.02	3.24	0.80	149.14	7.04	4.42	0.45	149.56	2.94
31	82.08038	35.78203	15.41	3.58	0.29	147.66	2.29	2.86	0.25	145.43	2.47	2.40	0.16	126.56	1.96	2.51	0.37	159.65	4.22
32	82.10609	35.77331	14.30	2.76	0.10	150.61	1.03	2.64	0.19	144.85	2.02	2.40	0.09	143.31	1.11	2.02	0.25	143.41	3.54
33	82.04495	35.74169	13.52	2.08	0.37	147.97	5.05	2.66	0.05	151.08	0.53	1.69	0.01	156.67	0.17	1.77	0.51	153.85	8.21
34[m]	82.02188	35.75947	14.11	2.92	0.42	149.60	4.13	2.38	0.05	147.45	0.63	3.64	0.16	149.65	1.24	2.94	0.76	152.60	7.38
35[m]	82.01313	35.79967	14.62	3.01	0.09	157.22	0.89	3.11	0.53	138.86	4.91	2.15	0.10	137.07	1.28	3.27	0.28	158.84	2.45
36	82.05405	35.77192	13.07	2.58	0.20	147.21	2.26	3.51	0.08	147.13	0.65	4.03	0.11	147.49	0.78	2.28	0.72	150.18	9.07
37[m]	82.05650	35.79475	13.80	2.95	0.26	159.66	2.49	2.96	0.06	148.05	0.62	-	-	-	-	2.90	0.31	155.12	3.03
38	82.02700	35.81169	12.30	2.84	0.27	162.24	2.80	2.13	0.10	144.42	1.31	2.74	0.17	163.21	1.81	2.56	0.18	151.20	2.00
39[v]	82.07225	35.82075	16.05	6.83	0.43	150.10	1.80	5.87	1.00	140.80	4.89	4.88	0.17	149.45	1.02	5.16	0.17	148.57	0.94
40	82.03321	35.77551	15.15	2.16	0.05	148.43	0.63	3.53	0.16	141.25	1.28	2.36	0.33	160.25	4.02	-	-	-	-
41[m]	82.32488	35.84697	16.24	2.18	0.19	162.46	2.55	1.39	0.21	148.61	4.23	1.51	0.05	133.31	0.96	2.01	0.02	174.49	0.23
42	82.29092	35.85814	15.74	1.74	0.05	147.52	0.80	-	-	-	-	1.62	0.23	144.45	4.09	2.16	0.20	146.08	2.62
43[m]	82.26075	35.85044	13.37	1.38	0.10	139.76	2.00	1.44	0.07	147.78	1.37	1.46	0.08	135.46	1.57	1.72	0.16	148.97	2.73
44	82.25704	35.83008	13.88	1.15	0.18	151.29	4.48	1.84	0.04	149.33	0.55	1.45	0.09	152.40	1.8	1.03	0.20	149.45	5.69
45	82.24479	35.85264	12.71	1.49	0.02	150.34	0.48	1.64	0.06	154.02	1.05	1.03	0.17	149.15	4.74	1.5	0.07	152.90	1.35
46	82.23921	35.83356	13.15	1.58	0.03	149.30	0.63	2.06	0.33	152.69	4.51	1.85	0.03	153.87	0.51	1.42	0.06	141.39	1.18
47	82.23542	35.81200	14.50	1.60	0.19	152.15	3.41	1.69	0.16	153.60	2.67	1.27	0.03	159.34	0.66	1.68	0.12	136.44	2.04
48	82.22788	35.81206	14.06	1.38	0.06	153.33	1.15	1.48	0.20	160.20	3.94	1.16	0.14	161.08	3.44	1.21	0.06	166.25	1.54
49	82.20692	35.82622	13.37	1.76	0.01	150.10	0.23	1.66	0.09	155.00	1.63	2.06	0.25	152.70	3.45	1.20	0.01	152.36	0.04
50	82.23338	35.87014	14.23	1.40	0.15	150.21	3.13	1.67	0.18	151.59	3.15	1.30	0.15	140.51	3.38	1.46	0.36	159.85	7.12
51	82.25325	35.89497	15.29	1.41	0.04	149.92	0.82	2.17	0.09	135.55	1.16	1.45	0.12	137.29	2.40	1.96	0.30	139.76	4.31
52	82.27100	35.89453	14.44	1.73	0.10	151.95	1.69	1.79	0.09	146.59	1.45	1.68	0.30	154.95	5.07	1.16	0.13	144.64	3.32
53	82.27817	35.89978	16.10	2.69	0.10	144.40	1.11	1.55	0.25	146.53	4.58	2.60	0.08	142.14	0.89	2.30	0.17	146.74	2.06
54	82.29571	35.90989	13.63	1.78	0.15	150.80	2.46	1.76	0.11	148.68	1.73	1.77	0.05	148.13	0.77	1.91	0.08	151.86	1.25
55	82.30146	35.91333	14.93	2.07	0.05	153.87	0.64	2.27	0.12	139.95	1.51	1.85	0.44	136.28	6.87	1.44	0.17	138.55	3.37
56	82.19350	35.89539	12.79	1.62	0.05	149.01	0.88	0.94	0.13	154.12	4.02	1.10	0.10	147.18	2.73	1.10	0.20	150.36	5.07
57	82.19458	35.83469	14.18	1.98	0.01	154.13	0.09	2.25	0.08	141.16	1.01	1.23	0.14	129.97	3.17	1.15	0.04	135.29	0.89
58	82.28158	35.93550	15.90	1.62	0.22	139.74	3.88	2.72	0.22	149.84	2.32	1.58	0.16	141.97	2.81	1.95	0.26	135.77	3.86
59[m]	82.20792	35.91392	14.25	2.43	0.22	143.83	2.62	2.08	0.25	152.64	3.43	1.68	0.19	137.25	3.21	1.70	0.01	147.19	0.03
60[m]	82.15113	35.86927	15.05	1.02	0.05	145.24	1.40	1.79	0.03	150.16	0.44	1.61	0.10	147.02	1.79	1.54	0.09	156.75	1.75
61	82.16342	35.85544	17.11	1.26	0.18	110.69	4.17	2.91	0.39	158.08	3.83	-	-	-	-	4.00	1.07	160.04	7.61
62	82.24539	35.68047	14.29	1.62	0.22	140.28	3.94	1.50	0.21	150.56	3.92	1.65	0.28	143.78	4.87	1.75	0.03	152.38	0.54
63	82.25054	35.69581	14.58	1.85	0.39	157.53	6.08	1.49	0.12	153.92	2.29	1.57	0.09	136.59	1.58	0.91	0.15	135.50	4.70
64	82.22925	35.68197	15.51	2.30	0.39	154.92	4.86	2.12	0.26	155.34	3.50	2.44	0.07	153.19	0.85	1.63	0.25	164.71	4.45
65	82.22846	35.69825	16.61	3.39	0.48	155.88	4.05	-	-	-	-	2.63	0.87	151.35	9.43	2.46	0.07	155.04	0.79
66	82.22262	35.66283	14.62	2.67	0.18	142.08	1.94	2.58	0.03	152.29	0.28	2.60	0.07	155.01	0.82	2.40	0.11	151.68	1.36
67	82.20958	35.66125	15.58	2.99	0.19	152.78	1.84	2.58	0.28	157.36	3.07	2.38	0.13	150.45	1.60	2.57	0.04	157.21	0.46
68	82.19058	35.66297	15.64	2.49	0.35	162.68	4.04	2.05	0.11	148.63	1.60	2.29	0.26	155.49	3.21	1.90	0.22	148.85	3.25
69[m]	82.20272	35.68189	15.40	0.75	0.08	155.55	3.07	2.50	0.41	150.17	4.74	2.57	0.23	145.28	2.57	-	-	-	-
70	82.20863	35.70406	16.03	3.96	0.04	151.08	0.31	3.66	0.01	136.94	0.05	3.71	0.13	138.73	1.02	3.47	0.09	141.69	0.73
71	82.20533	35.71397	15.44	1.70	0.45	139.74	7.57	2.00	0.04	146.86	0.61	3.05	0.02	159.08	0.23	2.00	0.47	152.50	6.80
72	82.19096	35.69861	13.97	1.37	0.30	139.67	6.19	2.25	0.11	146.14	1.43	2.26	0.14	142.03	1.81	2.14	0.22	135.60	2.99
73[m]	82.19813	35.73131	14.58	2.67	0.12	157.19	1.24	2.04	0.13	153.02	1.76	2.47	0.10	152.93	1.11	1.31	0.11	141.78	2.42
74[m]	82.18175	35.72303	13.27	3.08	0.01	152.46	0.10	2.77	0.10	149.79	1.00	3.26	0.06	150.81	0.50	1.49	0.26	145.47	4.96
75	82.17721	35.69739	14.74	2.77	0.23	144.75	2.39	2.25	0.15	148.90	1.85	3.39	0.12	146.94	1.03	1.69	0.27	147.64	4.57
76	82.17153	35.69247	14.87	3.16	0.22	155.77	1.96	3.27	0.03	156.55	0.24	2.94	0.12	149.83	1.18	3.04	0.01	149.13	0.05
77	82.17279	35.70108	14.01	3.04	0.38	151.46	3.54	3.03	0.06	141.22	0.57	3.48	0.08	153.39	0.70	2.58	0.23	144.23	2.60
78	82.19054	35.77289	13.55	1.90	0.10	154.57	1.46	2.67	0.07	144.65	0.74	2.74	0.07	152.62	0.78	1.77	0.18	145.44	2.92
79	82.21067	35.78003	12.82	1.48	0.24	147.94	4.55	1.98	0.04	147.50	0.61	1.28	0.33	154.15	7.41	1.18	0.13	156.18	3.08
80	82.23171	35.74903	12.54	1.29	0.03	151.38	0.67	1.36	0.11	155.50	2.41	1.30	0.10	147.27	2.16	2.07	0.36	150.10	5.02
81	82.22963	35.74592	15.27	2.70	0.60	153.08	6.33	2.47	0.23	141.78	2.62	2.29	0.12	157.71	1.49	1.27	0.40	145.14	9.07
82[m]	82.12998	35.66756	13.98	2.16	0.01	150.45	0.07	3.06	0.11	149.89	1.07	2.62	0.15	147.67	1.66	3.09	0.30	148.98	2.76
83	82.15172	35.68031	15.05	2.49	0.03	142.89	0.38	2.42	0.54	150.68	6.37	3.38	0.07	146.58	0.61	2.32	0.07	149.33	0.91
84	82.19358	35.64591	15.29	2.73	0.52	159.29	5.46	2.93	0.14	153.77	1.41	2.75	0.48	154.45	5.03	3.39	0.17	152.06	1.47
85	82.15693	35.70936	15.51	3.79	0.16	148.52	1.25	3.18	0.18	150.85	1.64	2.07	0.21	149.92	2.95	3.36	0.38	151.28	3.26
86[m]	82.22938	35.77481	14.86	1.71	0.07	150.45	1.24	1.00	0.22	164.10	6.38	1.13	0.05	152.33	1.34	1.11	0.27	2.44	6.84
87[m]	82.11793	35.71228	16.86	1.98	0.63	149.78	9.10	3.33	0.39	152.83	3.40	2.11	0.24	158.28	3.28	2.03	0.33	149.15	4.70
88	82.17592	35.73931	16.60	3.57	0.33	149.14	2.62	2.58	0.13	156.72	1.39	2.99	0.29	147.29	2.75	2.10	0.63	149.01	8.65
89[m]	82.16022	35.63325	16.55	4.16	0.14	161.71	0.98	2.71	0.81	150.82	8.55	3.32	0.13	152.37	1.11	3.72	0.76	139.21	5.85
90	82.15050	35.70990	17.82	8.00	0.01	154.94	0.01	5.61	0.67	143.96	3.42	6.36	0.99	147.65	4.46	5.55	1.63	155.13	8.36

[a] Classified as A6 III by Subramaniam & Sagar (1999)

[m] Member stars. Membership probabilities are listed in Table 4

[v] Classified as a variable star of unknown type by Li et al. (2021). Same as the star number #24 of Table 3

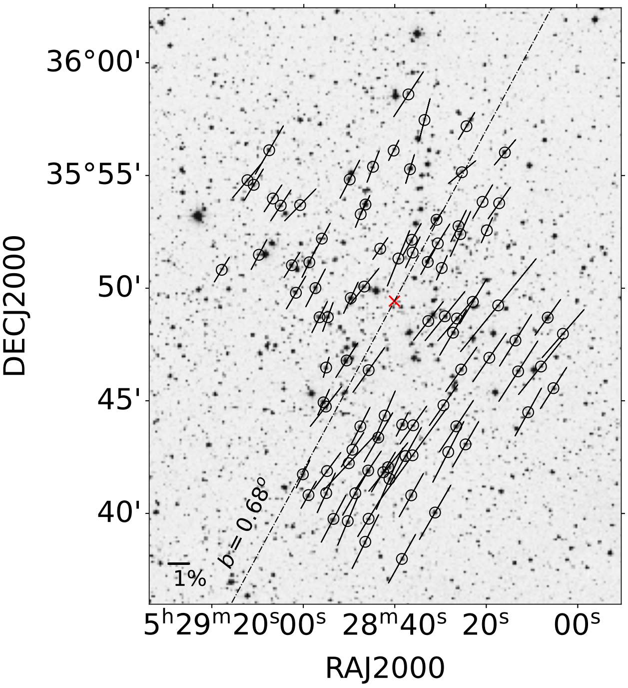

Figure 8. Polarization of the observed stars towards NGC 1912 in the V band superimposed on a 30′ × 30′ DSS R band image. The length of the polarization vectors is proportional to degree of polarization (in percentage). The inclination of the polarization vectors with respect to the north-south direction indicates the position angle of polarization. A line of magnitude of 1 per cent polarization value is drawn for reference. The dashed black line indicates the orientation of the projection of the Galactic plane at b = 0.68°. The red cross indicates the cluster centre at R.A. (J2000) = $05^h28^m40^s$ and Dec. (J2000) = +35°50′54″.

open-source code[5], developed by Almeida et al. (2023), the individual masses of the stars under polarimetric analysis were estimated, revealing that these stars have masses ranging approximately from 0.7 to 3 $M_\odot$.

5 DUST PROPERTIES

Studies such as McMillan (1978); Wilking et al. (1980) suggest that the wavelength (λ_{max}) corresponding to the maximum polarization (P_{max}) depends on the characteristic particle size distribution of aligned dust grains, in addition to their optical properties. Furthermore, it is also related to the interstellar extinction law (Whittet & Van Breda 1978; Coyne & Magalhaes 1979; Clayton & Cardelli 1988). To determine λ_{max} and P_{max}, we fitted the standard Serkowski's polarization law (Eq. 12) to the observed polarization in the BVR_cI_c wavelengths bands.

$$P_\lambda/P_{max} = exp\left[-kln^2(\lambda_{max}/\lambda)\right] \qquad (12)$$

The value of the parameter k is taken to be 1.15 (Serkowski 1973). Subsequent attempts to explore alternative values, such as $k = 1.66\lambda_{max} + 0.01$ (Whittet et al. 1992) and allowing k to be a free fit parameter (Bagnulo, Stefano et al. 2017), yielded unsatisfactory fits. σ_1 (the unit weight error of the fit) serves as a criterion for interstellar polarization and quantifies how closely our data aligns with the Serkowski relation. A value of σ_1 higher than 1.6 may suggest that the polarization has an intrinsic component (Medhi et al. 2007, 2008, 2010; Singh et al. 2020). Another parameter that could be indicative of the presence of intrinsic polarization and/or rotation of polarization angle along the line of sight (Coyne 1974; Martin 1974) is $\overline{\epsilon}$ when exceeding a threshold value of 2.3 (Eswaraiah et al. 2011). It is basically the polarization angle dispersion, normalized by the average of their associated errors (Marraco et al. 1993; Orsatti et al. 2007; Feinstein et al. 2008). Table 4 presents the best-fit values for P_{max}, λ_{max} along with their respective errors for a total of 87 stars. Additionally, the table also contains the following information: the *Gaia* ID for all the 90 stars that have been subjected to polarimetric analysis, value of σ_1 for 87 stars, $\overline{\epsilon}$ for 90 stars, the membership probability for 43 stars, and the distance, along with lower and upper bounds, for 85 stars. The distance to the stars were determined using the method discussed in Bailer-Jones et al. (2018), with updated parameters from *Gaia* DR3. Excluding the distance measurements with errors exceeding one-third of their respective values, we reported the individual distances for 85 stars out of the total 90 that were subjected to polarimetric analysis. We also computed P_{max}, λ_{max}, and σ_1 exclusively for stars that exhibit acceptable polarization levels ($P/e_P > 3$) in atleast three wavelength bands. A total of 87 stars meet this requirement, including 20 cluster members and 67 non-members (with 1 member and 2 non-member stars not meeting the criteria). Out of these 87 stars, only 34, including 10 members, exhibit σ_1 values below 1.6. Additionally, 28 stars, including 7 members, have $\overline{\epsilon}$ values exceeding 2.3. Notably, 21 stars (including 5 members), show both σ_1 greater than 1.6 and $\overline{\epsilon}$ surpassing 2.3, suggesting a higher probability of the presence of an intrinsic polarization component and/or rotation in polarization angle. Consequently, for NGC 1912, the observed polarization cannot be solely attributed to interstellar dust. Fig. 10 depicts the relationship between σ_1 and radial distance from the cluster center, for 87 polarimetrically analyzed stars. The black dash-dotted line represents $\sigma_1 = 1.6$. The scatter points are color-coded based on their $\overline{\epsilon}$ values. The members are indicated by red circles. The plot illustrates that a significant number of stars are potential candidates for intrinsic polarization. Typically, intrinsic polarization arises from asymmetrical circumstellar dust (for e.g., in binary systems) or electron scattering in classical Be stars (Orsatti et al. 2006). The reason for the large number of stars showing potential intrinsic polarization remains unclear, but it could be attributed to factors such as unresolved close binaries or rapid rotation. This idea might gain some credibility when considering star number #39 as listed in Table 3 (Same as star number #24 in Table A1). This star ($\sigma_1 = 3.63$ and $\overline{\epsilon} = 1.49$) is a potential candidate of intrinsic polarization and is identified by Li et al. (2021) as a variable star with an unknown classification. Also, Subramaniam & Sagar (1999) inferred from the CMD for cluster NGC 1912 that most of the stars in the cluster might be peculiar like fast rotators, binaries or stars with spots. Furthermore, Griggio et al. (2023) pointed out that the presence of unresolved binaries within the cluster constitutes one of the contributing factors to the color spread observed in the main sequence of NGC 1912. A considerable number of stars showing signs of intrinsic polarization were similarly observed in both the core and halo regions of NGC 6611 by Orsatti et al. (2006) and in IC 2944 by Vega et al. (1994). Orsatti et al. (2006) offered a possible explanation by using the work of Duchêne et al. (2001) on the total binary frequency of high-mass stars.

Figure 11 displays a plot of normalized polarization-wavelength dependence for the observed stars in NGC 1912. The black curve rep-

---

[5] accessible at `https://ocmass.streamlit.app/Detailed_MF`

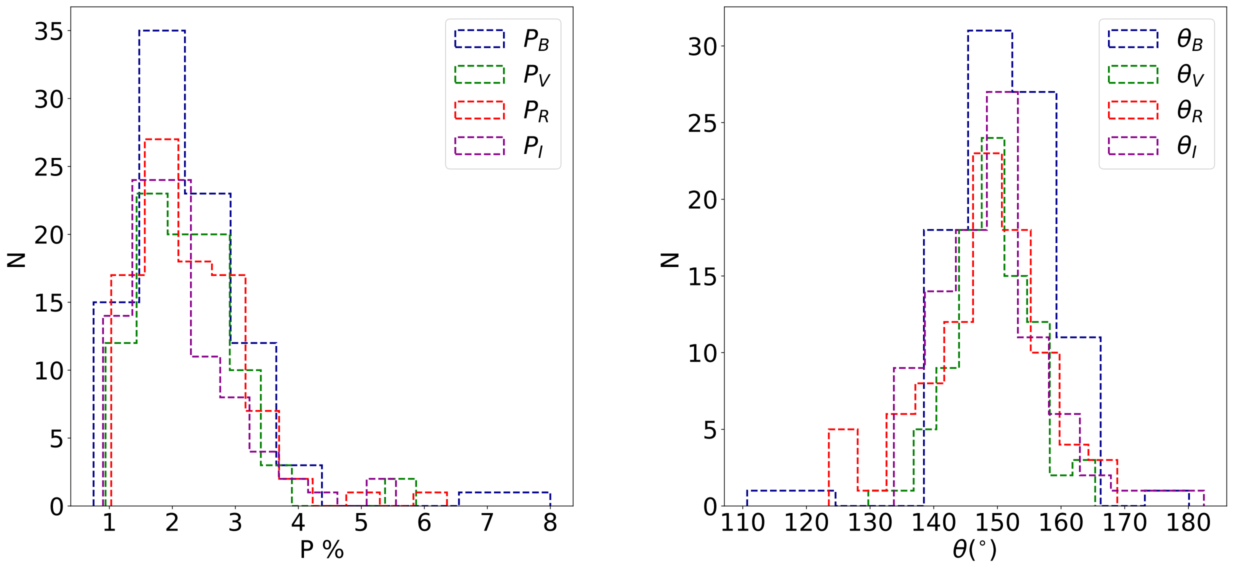

(a)

(b)

Figure 9. (a): Histogram of degree of polarization (in per cent). (b): Histogram of position angle of polarization (in degree). Position angles greater than 180° are reported as $(\theta - 180)^\circ$ in table 3.

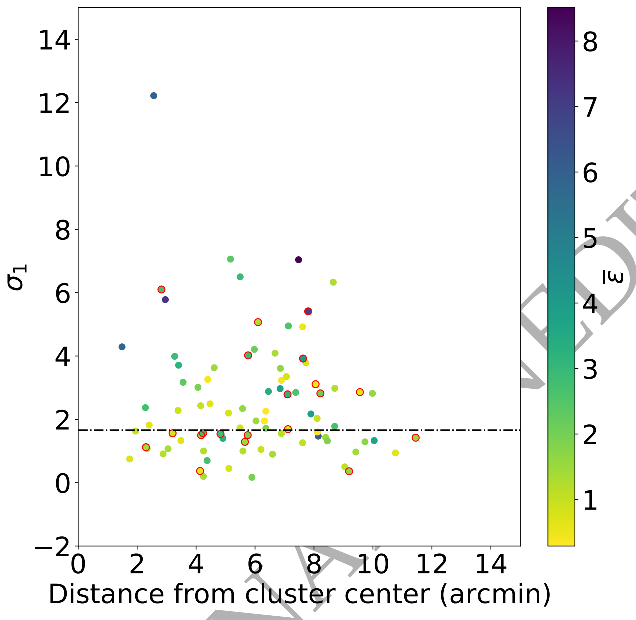

Figure 10. Plot of σ_1 against the distance (along the plane of the sky) from cluster center, for 87 (out of 90) polarimetrically analyzed stars. The scatter points are color coded according to their $\overline{\epsilon}$ value. The black dash-dotted line represents $\sigma_1 = 1.6$. The members of the cluster are enclosed in red circles

resents the Serkowski polarization relation for the general interstellar medium (ISM). We determined the co-efficient of determination (R^2) for the fit between the observed data and the serkowski polarization relation to be ≈ 0.38. The smaller value, indicating a suboptimal fit, could be attributed to the abundance of potential sources for intrinsic polarization and/or rotation in polarization angle.

Considering, stars with $\sigma_1 < 1.6$ and $\overline{\epsilon} < 2.3$, we calculate the weighted mean values of $P_{\rm max}$ and $\lambda_{\rm max}$ as 1.98 ± 0.28 per cent and 0.53 ± 0.03 μm, respectively. The inverse square of the errors associated with $P_{\rm max}$ and $\lambda_{\rm max}$ were used as weights in determining their averages, respectively. The value of total-to-selective extinction ratio given by $R_V = 5.6\lambda_{\rm max}$ (Whittet & Van Breda 1978), for the region is found to be 2.97 ± 0.17. According to Whittet (1977) the value of R_V can be represented by the relation $R_V = 3.08{+}0.17\sin(l{+}175^\circ)$. This gives the value of R_V towards NGC 1912 (l = 172.269) as ~ 3.04. Our estimate is in a close agreement with this value. The value of R_V obtained from ASteCA in the Sec. 3.3 also agrees well with these values.

Figure (12a) and (12b) illustrates the variation in both degree of polarization and position angle in the V band as a function of distance. The dash-dotted green line corresponds to the line of sight distance to the cluster, which is 1.096 Kpc. It is evident that precisely at the cluster distance, there are varying levels of polarization (in V-band) ranging from approximately 0.8 to 3.6 percent, accompanied by position angles ranging from approximately 138° to 166°. This observed fluctuation in polarization may be attributed to the candidates for intrinsic polarization as well as variations in dust concentrations within the region. The two dash-dotted red lines in Fig. (12a) and (12b) marks the distances of 1 kpc and 1.25 kpc. All the member stars, among those analyzed for polarimetry, lies within this distance range of 1 kpc - 1.25 kpc. We identified 21 stars (star number #2, #4, #6, #12, #13, #19, #27, #30, #31, #36, #39, #42, #55, #62, #70, #71, #72, #75, #77, #84, #88) lying beyond 1.25 kpc along the line of sight as background stars and 6 stars lying nearer than 1 kpc (star number #5, #14, #40, #49, #52, #85) as frontside stars.

For the member stars (with $\sigma_1 < 1.6$ and $\overline{\epsilon} < 2.3$) weighted mean values of $P_{\rm max}$ and $\lambda_{\rm max}$ are 1.85 ± 0.35 per cent and 0.47 ± 0.03

Table 4. GAIA ID, distance, membership probabilities and polarization results for the polarimetrically analysed stars towards NGC 1912

ID^{b}	*Gaia* ID	$P_{\max}$ (percent)	$e_{P_{\max}}$ (percent)	$\lambda_{\max}$ (μm)	$e_{\lambda_{\max}}$ (μm)	σ_1	$\overline{\epsilon}$	MP	d (pc)	d_{low} (pc)	d_{hi} (pc)
1	Gaia DR3 183352016427320320	2.65	0.15	0.76	0.06	1.95	1.51	0.46	1087.56	1067.76	1108.10
2	Gaia DR3 183352291309677312	2.34	0.30	1.09	0.13	4.09	1.35	…	1770.30	1487.39	2178.65
3^{a}	Gaia DR3 183352192527388032	…	…	…	…	…	0.44	…	1120.50	1068.64	1177.54
4	Gaia DR3 183350676397529600	1.82	0.10	0.53	0.07	1.82	0.62	…	1889.51	1818.26	1966.44
5	Gaia DR3 183363462520085120	2.12	0.21	0.76	0.12	0.17	2.02	…	844.21	817.80	872.36
6	Gaia DR3 183351677125407104	2.24	0.38	0.27	0.04	3.01	1.94	…	2275.89	2007.16	2623.89
7^{m}	Gaia DR3 183351608410353024	2.05	0.10	0.55	0.05	1.50	1.55	0.73	1095.84	1073.34	1119.23
8	Gaia DR3 183364252794039296	2.50	0.10	1.14	0.04	1.43	1.54	…	1152.47	1117.84	1189.27
9^{m}	Gaia DR3 183363733100785024	2.71	0.48	0.31	0.03	2.82	2.13	0.73	1104.54	1084.60	1125.21
10^{m}	Gaia DR3 183351093014240640	1.40	0.10	0.60	0.20	0.37	0.55	0.57	1080.64	1060.95	1101.06
11^{m}	Gaia DR3 183364145417644160	2.57	0.41	0.41	0.07	0.36	1.64	0.72	1109.40	1086.33	1133.44
12	Gaia DR3 183364115355068928	4.79	1.07	1.28	0.15	1.47	6.12	…	1680.34	1592.47	1778.26
13	Gaia DR3 183363561299412352	1.97	0.14	0.99	0.05	2.88	3.40	…	3017.60	2847.32	3208.98
14	Gaia DR3 183363634318784512	2.41	0.24	0.76	0.12	1.72	1.85	…	805.30	792.67	818.34
15	Gaia DR3 183351333532453760	2.30	0.04	0.71	0.02	12.22	5.97	0.04	1131.55	1110.95	1152.91
16^{m}	Gaia DR3 183351574050609536	2.09	0.19	0.47	0.06	1.56	0.78	0.73	1080.78	1060.33	1102.01
17^{m}	Gaia DR3 183351363592297600	1.83	0.12	0.88	0.06	2.37	2.76	0.01	1051.33	1032.88	1070.43
18	Gaia DR3 183351397953760384	1.58	0.03	0.48	0.03	1.12	2.04	0.66	1095.73	1069.31	1123.47
19	Gaia DR3 183339891739579264	3.87	0.75	0.22	0.02	7.06	2.38	…	1441.09	1399.22	1485.49
20	Gaia DR3 183351638471961088	2.21	0.05	0.89	0.02	0.70	2.70	…	1194.43	1171.83	1217.90
21	Gaia DR3 183327036897537920	2.43	0.13	0.58	0.08	0.75	0.73	0.34	1059.36	1037.08	1082.61
22	Gaia DR3 183323536504154112	1.81	0.03	0.92	0.03	6.50	2.95	0.13	1080.01	1057.30	1103.69
23	Gaia DR3 183323570863894912	3.18	0.13	0.50	0.04	2.34	1.62	…	...	...	...
24	Gaia DR3 183326182199693184	3.10	0.09	0.48	0.03	1.05	0.96	0.26	1098.06	1060.84	1137.92
25	Gaia DR3 183326594520874368	2.74	0.24	0.77	0.09	0.45	0.80	…	1138.36	1115.93	1161.69
26^{m}	Gaia DR3 183326010405340928	2.23	0.10	0.45	0.03	2.79	3.21	0.55	1085.45	1066.70	1104.86
27	Gaia DR3 183327758452043520	2.98	0.15	0.52	0.04	0.91	1.20	…	1766.43	1708.23	1828.65
28	Gaia DR3 183327002537800832	2.82	0.04	0.60	0.02	5.78	7.24	0.03	1172.80	1148.70	1197.92
29	Gaia DR3 183327758452043008	3.57	0.50	0.41	0.04	1.08	1.34	0.30	1089.41	1070.36	1109.14
30	Gaia DR3 183327827173169920	4.15	0.47	0.86	0.08	1.33	0.69	…	1923.45	1858.70	1992.78
31	Gaia DR3 183327247355901056	3.47	0.36	0.38	0.04	1.40	3.34	…	1956.31	1869.54	2051.33
32	Gaia DR3 183326869398775936	2.76	0.08	0.47	0.02	0.20	1.32	0.28	1049.44	1031.41	1068.09
33	Gaia DR3 183327071257284992	6.31	0.68	0.23	0.01	3.78	0.82	0.12	1193.23	1164.45	1223.44
34^{m}	Gaia DR3 183327346136707456	5.81	1.19	1.32	0.14	3.11	0.41	0.67	1112.90	1090.22	1136.52
35^{m}	Gaia DR3 183339204544866048	2.98	0.10	0.42	0.02	3.92	4.21	0.67	1069.07	1049.69	1089.16
36	Gaia DR3 183327277415712256	4.17	0.22	0.81	0.05	1.95	0.34	…	1871.01	1807.00	1939.64
37^{m}	Gaia DR3 183327522233810816	3.01	0.09	0.61	0.06	1.29	1.52	0.74	1094.49	1074.97	1114.73
38	Gaia DR3 183339307624072704	2.53	0.11	0.72	0.06	2.97	3.77	…	1067.34	1046.39	1089.13
39^{v}	Gaia DR3 183327930250733440	5.85	0.26	0.52	0.03	3.63	1.49	…	3958.17	3669.28	4294.59
40	Gaia DR3 183327384794872320	3.85	0.47	0.89	0.07	4.95	2.60	…	830.18	815.04	845.89
41^{m}	Gaia DR3 183349100149388544	2.24	0.11	1.10	0.07	5.41	5.89	0.73	1109.55	1074.63	1146.77
42	Gaia DR3 183349336369487872	2.07	0.11	0.65	0.04	2.26	0.31	…	2481.68	2242.12	2776.37
43^{m}	Gaia DR3 183347897558567808	1.53	0.06	0.65	0.05	1.54	2.81	0.68	1151.38	1117.62	1187.20
44	Gaia DR3 183347725759887104	1.83	0.08	0.47	0.04	3.26	0.39	0.08	1123.15	1099.04	1148.31
45	Gaia DR3 183350852496072448	1.62	0.03	0.58	0.02	2.43	0.97	…	1039.48	1014.28	1065.95
46	Gaia DR3 183347790179508608	1.80	0.02	0.60	0.01	3.17	2.32	…	1112.13	1071.61	1155.79
47	Gaia DR3 183347691400163456	1.36	0.07	0.56	0.07	3.71	3.18	…	1106.29	1085.09	1128.33
48	Gaia DR3 183347377862651392	1.43	0.05	0.53	0.03	1.07	1.37	0.29	1181.74	1140.16	1226.39
49	Gaia DR3 183350337100020608	1.76	0.01	0.45	0.01	1.63	0.98	…	776.47	765.44	787.81
50	Gaia DR3 183350916915697024	1.50	0.09	0.53	0.08	1.00	1.23	…	1085.16	1059.88	1111.66
51	Gaia DR3 183352433039544064	1.87	0.11	0.70	0.04	4.21	2.14	…	…	…	…
52	Gaia DR3 183352398684268928	1.79	0.08	0.46	0.04	0.90	1.36	…	828.54	816.20	841.26
53	Gaia DR3 183352398684262528	2.70	0.07	0.53	0.02	3.35	0.78	…	1177.45	1140.75	1216.53
54	Gaia DR3 183352531823397120	1.84	0.04	0.67	0.04	2.03	0.94	…	1099.92	1059.55	1143.42
55	Gaia DR3 183352536123202560	2.12	0.05	0.49	0.03	1.32	1.89	…	2035.94	1950.23	2129.36
56	Gaia DR3 183351848928483456	1.72	0.12	0.34	0.03	2.49	0.65	0.44	1066.44	1044.26	1089.56
57	Gaia DR3 183350405819497856	2.00	0.01	0.41	0.01	4.29	5.82	0.04	1081.40	1058.96	1104.79
58	Gaia DR3 183352811001106560	2.00	0.12	0.55	0.07	2.98	1.27	0.26	1063.38	1045.34	1082.03
59^{m}	Gaia DR3 183351986367421312	2.25	0.16	0.49	0.03	1.50	2.02	0.58	1091.36	1071.75	1111.69
60^{m}	Gaia DR3 183351470971385856	1.86	0.06	0.76	0.03	6.10	2.72	0.61	1161.82	1083.51	1252.06
61	Gaia DR3 183351402251911552	…	…	…	…	…	3.10	0.49	1168.57	1137.31	1201.57
62	Gaia DR3 183322265193828608	1.79	0.06	0.69	0.06	0.97	1.42	…	1346.35	1314.92	1379.28
63	Gaia DR3 183322363973132672	1.72	0.21	0.44	0.06	1.78	2.69	0.29	1127.47	1102.62	1153.44
64	Gaia DR3 183322333913310464	3.39	0.40	0.49	0.05	0.50	1.12	0.18	1058.99	1037.89	1080.96
65	Gaia DR3 183322540071733504	3.38	0.57	0.47	0.04	1.60	0.29	…	...	...	...
66	Gaia DR3 183322157814705280	2.61	0.03	0.59	0.02	1.33	3.72	…	1205.56	1179.66	1232.60
67	Gaia DR3 183322192175740288	2.84	0.09	0.58	0.03	2.82	1.63	…	1083.21	1035.80	1135.07
68	Gaia DR3 183322024675682816	2.14	0.09	0.56	0.07	1.29	1.71	0.07	1056.68	1037.63	1076.43
69^{m}	Gaia DR3 183322402632794880	…	…	…	…	…	0.75	0.57	1093.53	1069.10	1119.08
70	Gaia DR3 183322608791213952	3.76	0.02	0.48	0.01	7.04	8.51	…	4034.27	3730.62	4389.63
71	Gaia DR3 183322608791211776	7.06	0.68	1.56	0.07	3.61	1.64	…	1825.27	1761.23	1894.05
72	Gaia DR3 183322501412085760	2.29	0.11	0.69	0.07	1.26	1.04	…	2275.65	2129.43	2442.88
73^{m}	Gaia DR3 183323429125018752	2.66	0.12	0.41	0.02	4.02	2.89	0.73	1136.74	1112.02	1162.57
74^{m}	Gaia DR3 183323330345720192	3.23	0.03	0.54	0.01	5.07	1.27	0.62	1097.40	1067.91	1128.54
75	Gaia DR3 183323227266516736	2.90	0.09	0.64	0.05	4.92	0.49	…	1360.02	1330.41	1390.95
76	Gaia DR3 183323227266520704	3.31	0.02	0.61	0.01	2.17	3.90	0.04	1172.98	1145.00	1202.32
77	Gaia DR3 183323222966591232	3.31	0.08	0.70	0.04	2.85	2.62	…	1847.53	1777.90	1922.71
78	Gaia DR3 183347206063965568	2.64	0.06	0.67	0.03	3.99	2.90	…	1109.90	1079.51	1142.00
79	Gaia DR3 183347176004112640	2.11	0.14	0.42	0.04	2.28	0.95	…	1031.40	991.77	1074.26
80	Gaia DR3 183346901126213504	1.40	0.06	0.58	0.04	1.73	0.93	…	…	…	…
81	Gaia DR3 183346862466584448	2.76	0.42	0.43	0.07	1	1.22	0.17	1175.21	1150.12	1201.38
82^{m}	Gaia DR3 183322780590377216	3.04	0.14	0.76	0.03	2.86	0.66	0.60	1060.85	1039.44	1083.14
83	Gaia DR3 183322814949673216	2.89	0.04	0.62	0.01	6.33	1.27	0.01	1056.49	1030.76	1083.50
84	Gaia DR3 183321814217322368	3.35	0.15	0.77	0.06	0.94	0.66	…	1755.40	1696.26	1818.73
85	Gaia DR3 183323295985995008	3.90	0.28	0.36	0.03	3.23	0.40	…	902.68	885.95	920.04
86^{m}	Gaia DR3 183347072924892416	1.79	0.13	0.35	0.02	1.56	2.77	0.72	1094.72	1073.02	1117.29
87^{m}	Gaia DR3 183323158547052672	2.69	0.40	0.47	0.09	1.69	0.59	0.73	1125.11	1091.98	1160.27
88	Gaia DR3 183323639583361024	3.02	0.31	0.42	0.07	2.20	0.80	…	1413.80	1363.32	1468.07
89^{m}	Gaia DR3 183321848578281984	4.14	0.15	0.43	0.02	1.42	1.46	0.70	1103.98	1078.10	1131.11
90	Gaia DR3 183323124187305088	8.50	0.56	0.35	0.04	1.55	1.14	…	…	…	…

[b] This ID is same as Table 3

Superscripts a, m and v has same meaning as Table 3.

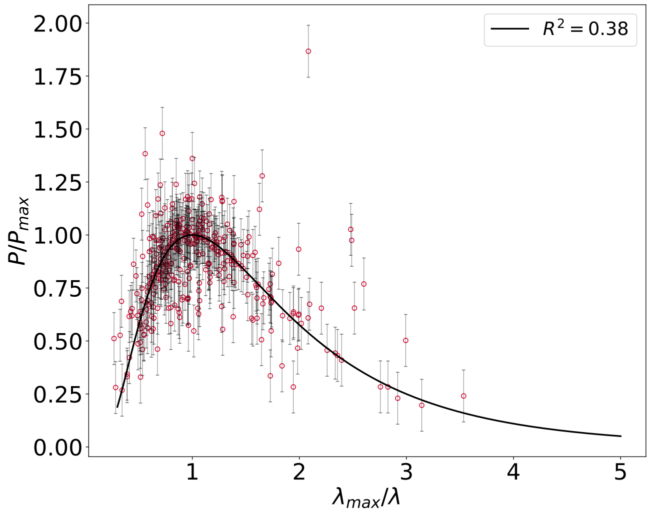

Figure 11. The plot of $P/P_{\max}$ against $\lambda_{\max}/\lambda$ showing the normalized polarization-wavelength dependence for the observed stars in NGC 1912.The uncertainties for the measurements of $P/P_{\max}$ are represented by the error bars and the solid curve reflects the Serkowski polarization relation for general diffuse ISM. The co-efficient of determination (R^2) of the fit between the observed data and serkowski's relation is shown in the top right corner.

μm. Corresponding values for the frontside stars (with $\sigma_1 < 1.6$ and $\bar{\epsilon} < 2.3$) are 1.83 ± 0.15 per cent and 0.48 ± 0.14 μm and for background stars, the values are 2.14 ± 0.42 per cent and 0.59 ± 0.06 μm. For the polarization, which is dominated by dust particles present in the diffuse ISM, the value of $\lambda_{\max}$ lies nearly at 0.55 μm (Serkowski et al. 1975). Considering the calculated $\lambda_{\max}$ values, it is reasonable to conclude that the dust grains responsible for polarizing the member stars of the cluster (that lie within the distance range of 1 kpc - 1.25 kpc) are comparatively smaller than that of the general ISM. The reason behind this might be the evaporation of the dust particles due to the presence of some massive stars in the central region of the cluster. On the other hand, the dust grains responsible for polarizing the background stars are almost similar to that of the general ISM. It is difficult to derive a conclusion in this regard for the frontside stars as because $\lambda_{\max}$ value for the foreground stars show large statistical error mainly due to the small number (only 6) of foreground stars detected.

6 DUST DISTRIBUTION AND SECONDARY STAR FORMATION

To understand the dust distribution within and around the polarimetrically observed region of the cluster NGC 1912, we generated an extinction map of the region towards the cluster using JHK_s NIR data from the 2MASS point source catalog (Cutri et al. 2003; Skrutskie et al. 2006) within a field of view 35 x 35 arcmin^2. We used the PNICER technique (Meingast et al. 2017), which characterizes extinction through a probability density function. PNICER estimates extinction by fitting Gaussian mixture models along the extinction vector, based on control field (extinction free) observations. PNICER is offered to the community as an open-source software solution and is entirely written in Python. Additionally, we validated the extinction map using the well-established NICER (Lombardi & Alves 2001; Lombardi et al. 2006, 2008; Lombardi et al. 2011; Alves et al. 2014) technique which is accessible through the PNICER software package. We have overplotted the contours with levels 12, 15, 35, 40, 45,50 and 55 counts pixel^{-1} extracted from *Herschel SPIRE* 500μm dust continuum emmission on the extinction map. It is clearly evident from Figure (13a) that the contours are in an excellent agreement to the extinction map of the region. The polarization vectors in the V band were overplotted on the extinction map and are shown in Fig. (13a). The color bar on the right side of the figure shows the range of A_{k_s} from 0 to 0.30. The reference polarization vector for 1 per cent polarization is shown towards the left.

The area under polarimetric observation shows low overall extinction, indicating a low concentration of dust. This observation also suggests that fewer stars in this region are likely to exhibit polarization only due to interstellar dust. However, certain areas within the observed region exhibit relatively higher extinction, indicating the possibility of differential extinction within the cluster region. It can be clearly seen from Fig. (13a) the extinction towards the central and eastern part of this region is relatively lower compared to other regions. This may be due to the effects associated with massive stars (de Geus 1991). We detected the presence of three B-type (Mel'nik & Dambis 2017) stars towards the eastern part of NGC 1912 : (i) BD +35 1169 (R.A. (J2000) = 05^{h}34^{m}21.69^s, Dec. (J2000) = +35°48′48.93″; spectral type = B1) (ii) HD 35952 (R.A. (J2000) = 05^{h}29^{m}57.61^s, Dec. (J2000) = +35°57′17.10″; spectral type = B5) (iii) BD +35 1141 (R.A. (J2000) = 05^{h}29^{m}59.12^s, Dec. (J2000) = +35°12′09.63″; spectral type = B0.5). They are not the members of the cluster. Their distance estimates from Bailer-Jones et al. (2018) show that they are located somewhat towards the background of the cluster. These stars are highlighted in Fig. (13b). Feedback mechanisms from such massive stars, (radiation, stellar winds, and supernovae), can disperse the surrounding materials, leading to the formation of void-like structures known as "interstellar bubbles" (Weaver et al. 1977). A similar void, possibly formed due to the aforementioned feedback processes, is evident towards the eastern region in the extinction map depicted in Fig. (13a). To further investigate, Fig. (13b) presents a 4° × 4° AKARI WIDE-S (90 μm) dust emission colormap of the region centered at R.A. = 05^{h}32^{m}20.4^s; Dec = +35°43′29″, with a contour of 20 counts pixel^{-1}, which clearly shows the probable bubble region.

Now, in order to investigate the star formation scenario in our region of the polarimetric study, we conducted an identification of young stellar objects (YSOs), using the NIR two-color diagram (TCD), illustrated in Fig. (14). The blue solid curve represents the unreddened main sequence (Koornneef 1983), while the two dash-dotted purple lines indicate the reddening vector (Rieke & Lebofsky 1985). The black dashed line represents the de-reddened classical T Tauri locus (Meyer et al. 1997). The region to the right of the reddening band, known as the NIR excess region, corresponds to the location of YSOs, primarily classical T Tauri stars (CTTSs) with significant NIR excesses (Sheikh & Medhi 2024). We acquired NIR JHK_s data from the 2MASS point source catalog (Cutri et al. 2003) for stars within a 35 arcmin box centered around NGC 1912, covering the area that was subjected to the polarimetric analysis. This box size was chosen to focus on the cluster's central region, where evidence of massive stars is prominent and hence the chances of star formation activities are greater. Stars with line-of-sight distances less than 1 kpc and greater than 1.25 kpc were excluded to filter out nearby foreground and distant background stars leaving us with 743 stars that lie within the extents of the cluster. These are shown in Fig. (14) with gray filled circles. From this plot, we identified 16 probable YSOs in the region of the cluster, that are highlighted by green circles. Out of these 16 candidate YSOs identified, 2 of them are found to be member stars of cluster NGC 1912 and out of 14 remaining

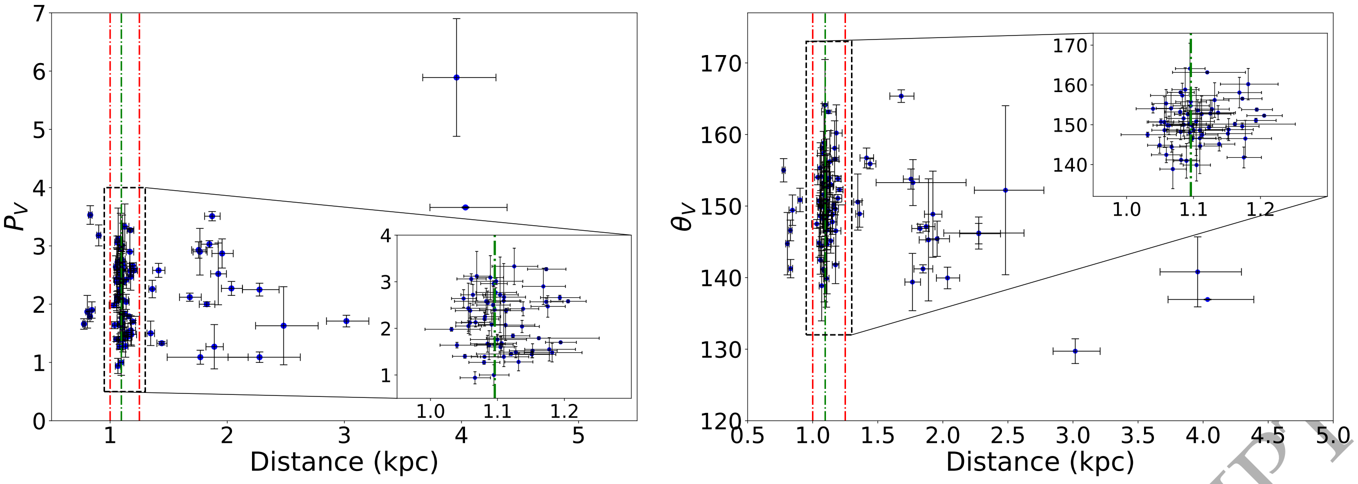

(a)

(b)

Figure 12. (a): The plot of degree of polarization (in per cent) of the stars against their distance (in Kpc) with zoomed view of the region between 1kpc and 1.25kpc.(b): The plot of position angle of polarization (in degree) of the stars against their distance (in Kpc) with zoomed view of the region between 1kpc and 1.25kpc. In the figures the two dash-dotted red lines indicate distances of 1 kpc and 1.25 kpc while the green dash-dotted line indicates the distance to the cluster NGC 1912 (1.096 Kpc).

non-member YSOs, 3 of them have been polarimetrically analyzed and they correspond to star no. #13, #65 and #90 of Table 3. These have been highlighted in detail in Fig. (14) as well as Fig. (13a).

Interestingly, as it can be seen from Fig. (13b), the 16 candidate YSOs are located in the peripheral regions of the proposed interstellar bubble. These are depicted in Fig. (13b) using black star symbols. This observation is strikingly consistent with the theory that the peripheral accumulation of materials around a bubble can trigger secondary star formation (Kim et al. 2021). The non-spherical shape of the apparent bubble obtained in this region, as evident from Fig. (13b), is consistent with the findings of van Marle, A. J. et al. (2015) which states that low magnetic fields found in galactic disks inhibit the growth of the bubble in the direction perpendicular to that of the field thus giving rise to an ovoid shape rather than spherical.

7 RESULTS, SUMMARY AND DISCUSSION

This study offers a comprehensive investigation of the low-galactic latitude cluster, NGC 1912, situated towards the anti-galactic center direction. The cluster has been characterized in context of its fundamental and structural parameters, mass distribution, dust properties and the star formation dynamics. In order to achieve this goal, rigorous statistical techniques have been incorporated into polarimetric, photometric and astrometric data. The following text presents a comprehensive overview of our findings.

The membership analysis, in this work, identified 401 cluster members for NGC 1912, with mean values of parallax and two proper motions, calculated as $\overline{\pi}$ = 0.877 ± 0.001 mas, $\overline{\mu_\alpha cos\delta}$ = 1.533 ± 0.004 mas yr^{-1} and $\overline{\mu_\delta}$ = -4.434 ± 0.005mas yr^{-1}. Fitting the King (1962) function to the observed radial surface density profile of the cluster, provided the values of structural parameters as : central density (ρ_o) = 0.643 ± 0.067 stars arcmin^{-2}, core radius (r_c) = 7.743 ± 0.784 arcmin, tidal radius (r_t) = 84.633 ± 7.188 arcmin, and background density (ρ_{bg}) = 0.001 ± 0.000 stars arcmin^{-2}. The fundamental parameters characterizing the cluster NGC 1912 were determined as : Metallicity (z) = 0.0141 ± 0.0006, Age = 330 ± 30 Myr, Binary fraction (b_{frac}) = 0.445 ± 0.035, Visual extinction (A_V) = 0.864 ± 0.033 mag, Total-to-selective extinction ratio (R_V) = 3.007 ± 0.096, distance = 1096 ± 15 pc.

The study also investigates the scenario of dynamical mass segregation within the cluster revealing a concentration of relatively massive stars towards the cluster center.

Furthermore, polarimetric observations were reported for 90 stars towards NGC 1912 in BVR_cI_c wavelength bands. Out of 90, only 21 stars have been found to have a membership probability greater than 0.5. It was found that polarization for NGC 1912 is not just due to interstellar dust alone. Many stars showed potential intrinsic polarization and/or rotation in position angle, probably due to factors like unresolved close binaries or rapid rotators. Also, it was found that the polarization position angle of polarimetrically analyzed stars nearly align to the Galactic Plane, suggesting the dominance of galactic magnetic field in the region of polarimetric observation. Calculations of $\lambda_{\max}$ (Wavelength at which maximum polarization occurs) revealed that the dust grain sizes within the intra-cluster region are comparatively smaller than that of the general ISM. This might be due to the presence of the relatively massive stars, towards the center of the cluster, which could lead to the evaporation of dust particles.

The extinction map of region towards NGC 1912 revealed that the area under polarimetric observation exhibits an overall low concentration of dust. Possibilities of differential extinction in the region was detected. It was found that the eastern and central part of the cluster has relatively lower dust content.The cause of this could be attributed to the effects associated to massive stars located eastwards of the cluster. Interestingly, we also detected the existence of a potential "interstellar bubble", located in the vicinity of the cluster region, possibly formed due to the feedback from the massive stars. The possible bubble region is found to exhibit an ovoid-like geometry. Towards the peripheral region of the bubble, we found 16 probable YSOs, primarily classical T Tauri stars, suggesting triggered secondary star formation in the region.

Notably, the immediate neighborhood of the proposed bubble re-

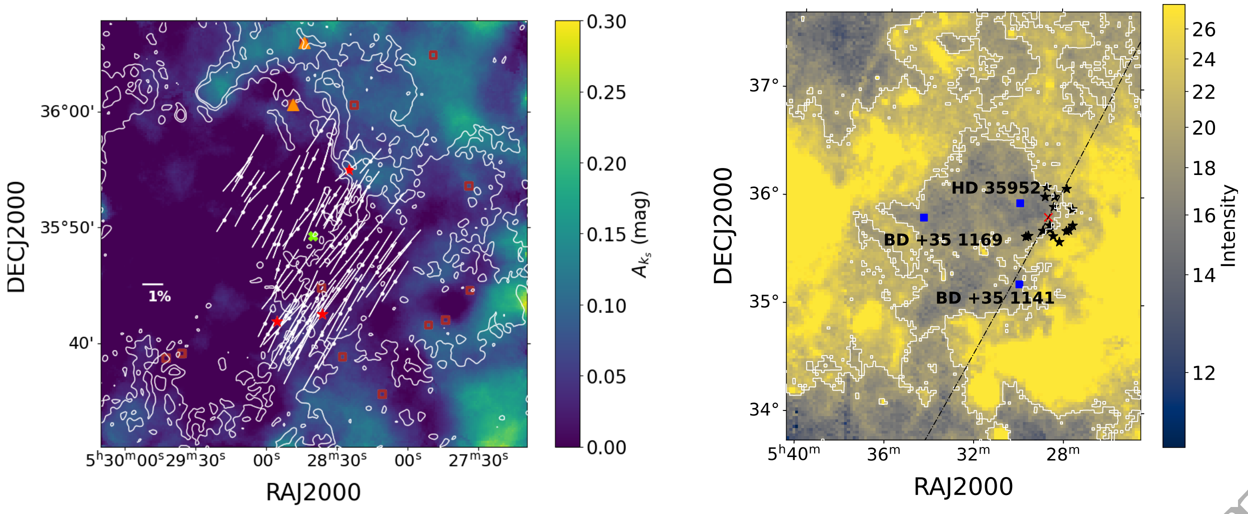

(a) (b)

Figure 13. (a) PNICER extinction map of NGC 1912 within a FoV of 35' X 35'. The green cross represents the cluster center [R.A. = $05^h28^m40^s$; Dec = +35°50′54″]. The contours, with levels 12, 15, 35, 40, 45,50 and 55 counts pixel^{-1}, extracted from *Herschel SPIRE* 500μm dust continuum emmission and the polarization vectors are overplotted on the extinction map. The reference polarization vector for 1 per cent polarization is shown towards the left. 16 probable YSOs comprising of 2 member stars (orange triangles) and 14 non-members (brown unfilled squares) including 3 polarimetrically analyzed YSOs (red star symbol) are also shown in the figure. (b) 4° × 4° AKARI WIDE-S (90 μm) dust emission color map of the region centered at R.A. = $05^h32^m20.4^s$; Dec = +35°43′29″ with a contour of 20 counts pixel^{-1} constructed using matplotlib package in python showing the proposed bubble region. The red cross represents the center of the cluster NGC 1912. The black star symbols represent the probable YSOs identified from the NIR TCDs for NGC 1912. The blue square symbols indicate three B-type stars with their names annotated, that are located eastwards of the cluster NGC 1912.

gion lacks evidence of an HII region. The nearest HII region found, IC 417 (also known as LBN 173.46-00.16 and SH 2-234; l = 173.38°, b = - 0.20°), is located at an angular distance of ≈ 85.08 arc min from the center of the cluster NGC 1912. This emphasizes the importance of conducting a comprehensive multi-wavelength photometric and spectroscopic analysis of the proposed bubble region in the future. Such an analysis coupled with the study of star formation dynamics across its entire periphery, will be crucial to confirm the presence of the "interstellar bubble" within this region.

ACKNOWLEDGEMENTS

The authors are grateful to the anonymous referee for their constructive comments. We express our gratitude to the Aryabhatta Research Institute of Observational Sciences (ARIES), Nainital, for providing telescope time. We would also like to acknowledge the *Herschel* Science Archive from which we downloaded the *Herschel* SPIRE 500 μm map in the region of NGC 1912. This research has made use of the VizieR catalogue access tool, CDS, Strasbourg, France, the WEBDA database, operated at the Department of Theoretical Physics and Astrophysics of the Masaryk University, Digitized Sky Survey (DSS), which was produced at the Space Telescope Science Institute under the US Government grant NAG W-2166, NASA's Astrophysics Data System, observations made with the Galaxy Evolution Explorer, obtained from the MAST data archive at the Space Telescope Science Institute, which is operated by the Association of Universities for Research in Astronomy, Inc., under NASA contract NAS 5–26555, data from the the European Space Agency (ESA) mission Gaia `https://www.cosmos.esa.int/gaia`, processed by the Gaia Data Processing and Analysis Consortium (DPAC, `https://www.cosmos.esa.int/web/gaia/dpac/consortium`). Funding for the DPAC has been provided by national institutions, in particular the institutions participating in the Gaia Multilateral Agreement. We made use of IRAF, distributed by National Optical Astronomy Observatories, USA. The author SB highly acknowledges the Department of Science and Technology (DST), Govt. of India for providing DST INSPIRE fellowship vide grant no. IF220155. The authors extend their sincere gratitude towards Stefan Meingast, Coryn Bailer-Jones and Sadhana Singh for their valuable suggestions in improving this work.

DATA AVAILABILITY

The multi-wavelength photometric data underlying this article are publicly available at Gaia Archive, 2MASS Point Source Catalog, Herschel Science Archive and MAST Data Discovery Portal. The polarimetric data derived in this research will be shared on reasonable request to the corresponding author.

REFERENCES

Agarwal M., Rao K. K., Vaidya K., Bhattacharya S., 2021, MNRAS, 502, 2582
Almeida A., Monteiro H., Dias W. S., 2023, MNRAS, 525, 2315
Alves J., Lombardi M., Lada C. J., 2014, A&A, 565, A18
Bagnulo, Stefano et al., 2017, A&A, 608, A146
Bailer-Jones C. A. L., Rybizki J., Fouesneau M., Mantelet G., Andrae R., 2018, AJ, 156, 58
Balaguer-Núñez L., et al., 2020, MNRAS, 492, 5811
Becker W., 1963, Z. Astrophys., 57, 117
Bhattacharya S., Mahulkar V., Pandaokar S., Singh P., 2017, Astronomy and Computing, 18, 1
Bianchi L., 2009, Ap&SS, 320, 11
Bodenheimer P., 1997, in Pendleton Y. J., ed., ASP Conf. Ser. Vol. 122, From Stardust to Planetesimals. p. 37

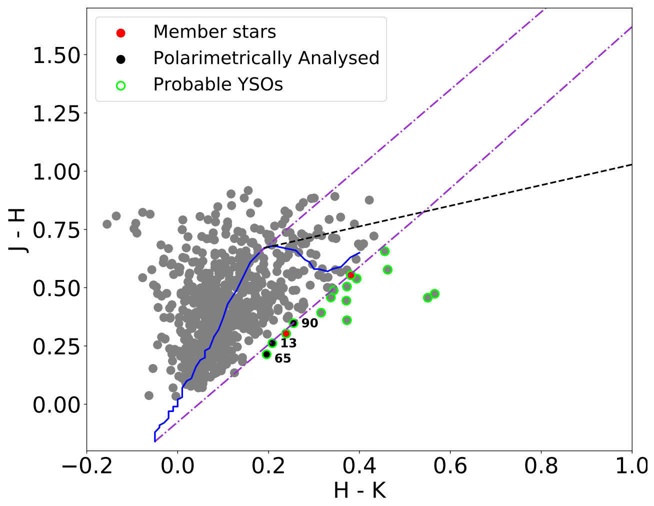

Figure 14. NIR two color diagram (TCD) for all the stars (filled gray circles) within a box of size 35 arc-min around NGC 1912 and within a distance range of 1Kpc and 1.25 Kpc. The green circles indicate the probable candidates of Young Stellar objects (YSOs). Red circles show the YSOs which are also member stars of NGC 1912. Black circles show the YSOs which have been polarimetrically analysed . The numbers annotated on the black circles correspond to the IDs listed in Table 3. The blue solid curve indicates the unreddened main sequence (Koornneef 1983). The two dash-dotted purple lines indicate the redenning vector (Rieke & Lebofsky 1985). The black dashed line represents the de-redenned classical T Tauri locus (Meyer et al. 1997)

Bressan A., Marigo P., Girardi L., Salasnich B., Dal Cero C., Rubele S., Nanni A., 2012, MNRAS, 427, 127
Cantat-Gaudin T., et al., 2018, A&A, 618, A93
Castro-Ginard A., et al., 2020, A&A, 635, A45
Chen Y., Bressan A., Girardi L., Marigo P., Kong X., Lanza A., 2015, MNRAS, 452, 1068
Clayton G. C., Cardelli J. A., 1988, AJ, 96, 695
Cordoni G., et al., 2023, A&A, 672, A29
Cover T., Hart P., 1967, IEEE Transactions on Information Theory, 13, 21
Coyne G., 1974, AJ, 79, 565
Coyne G., Magalhaes A., 1979, AJ, 84, 1200
Cutri R. M., et al., 2003, VizieR Online Data Catalog, p. II/246
Das H. S., Medhi B. J., Wolf S., Bertrang G., Deb Roy P., Chakraborty A., 2013, MNRAS, 436, 3500
Davis Jr L., Greenstein J. L., 1951, ApJ, 114, 206
De Graauw T., et al., 2010, A&A, 518, L6
De Oliveira M., Fausti A., Bica E., Dottori H., 2002, A&A, 390, 103
Deb Roy P., Halder P., Das H. S., Medhi B. J., 2015, MNRAS, 450, 1770
Deb S., Baruah A., Kumar S., 2022, MNRAS, 515, 4685
Deisenroth M. P., Faisal A. A., Ong C. S., 2020, Mathematics for machine learning
Dias W., Lépine J. R. D., Alessi B., 2002a, A&A, 388, 168
Dias W., Alessi B., Moitinho A., Lépine J., 2002b, A&A, 389, 871
Dias W., Monteiro H., Caetano T., Oliveira A., 2012, A&A, 539, A125
Dias W. S., Monteiro H., Caetano T. C., Lépine J. R. D., Assafin M., Oliveira A. F., 2014, A&A, 564, A79
Dias W. S., Monteiro H., Lépine J. R. D., Prates R., Gneiding C. D., Sacchi M., 2018, Monthly Notices of the Royal Astronomical Society, 481, 3887
Dias W. S., Monteiro H., Moitinho A., Lépine J. R. D., Carraro G., Paunzen E., Alessi B., Villela L., 2021, MNRAS, 504, 356
Donor J., et al., 2020, AJ, 159, 199
Duchêne G., Simon T., Eislöffel J., Bouvier J., 2001, A&A, 379, 147
El Aziz M. A., Selim I. M., Essam A., 2016, Experimental Astronomy, 42, 49
Elson R. A. W., Fall S. M., Freeman K. C., 1987, ApJ, 323, 54
Eswaraiah C., Pandey A., Maheswar G., Medhi B. J., Pandey J., Ojha D., Chen W., 2011, MNRAS, 411, 1418
Feinstein C., Vergne M. M., Martínez R., Orsatti A. M., 2008, MNRAS, 391, 447
Foreman-Mackey D., Hogg D. W., Lang D., Goodman J., 2013, PASP, 125, 306
Friel E., 1995, ARA&A, 33, 381
Fu X., et al., 2022, A&A, 668, A4
Gaia Collaboration et al., 2018, A&A, 616, A1
Gaia Collaboration et al., 2021a, A&A, 649, A1
Gaia Collaboration et al., 2021b, A&A, 649, A1
Gaia Collaboration et al., 2023, A&A, 674, A41
Gao X., 2014, RAA, 14, 159
Gao X., 2018, AJ, 156, 121
Gao X., 2019, MNRAS, 486, 5405
Gao X., 2020, Ap&SS, 365, 24
Girardi L., Bertelli G., Bressan A., Chiosi C., Groenewegen M. A. T., Marigo P., Salasnich B., Weiss A., 2002, A&A, 391, 195
Girichidis P., et al., 2020, Space Sci. Rev., 216, 1
Griffin M. J., et al., 2010, A&A, 518, L3
Griggio M., Salaris M., Bedin L. R., Cassisi S., 2023, MNRAS, 523, 5148
Hidalgo S. L., et al., 2018, The Astrophysical Journal, 856, 125
Hirashita H., Ferrara A., 2002, MNRAS, 337, 921
Hirashita, H. Hunt, L. K. 2004, A&A, 421, 555
Hoag A. A., Applequist N. L., 1965, ApJS, 12, 215
Høg E., et al., 2000, A&A, 355, L27
Hunt E. L., Reffert S., 2021, A&A, 646, A104
Hunt E. L., Reffert S., 2023, A&A, 673, A114
Jacobson H. R., Cummings J., Deliyannis C. P., Steinhauer A., Sarajedini A., 2002, in American Astronomical Society Meeting Abstracts. p. 124.07
Johnson H. L., Hoag A. A., Iriarte B., Mitchell R. I., Hallam K. L., 1961, Lowell Observatory Bulletin, 5, 133
Kharchenko N. V., 2001, Kinematika i Fizika Nebesnykh Tel, 17, 409
Kharchenko N., Piskunov A., Röser S., Schilbach E., Scholz R.-D., 2005, A&A, 438, 1163
Kim S., Lim B., Bessell M. S., Kim J. S., Sung H., 2021, AJ, 162, 140
King I., 1962, AJ, 67, 471
Koornneef J., 1983, A&AS, 51, 489
Krone-Martins A., Moitinho A., 2014, A&A, 561, A57
Lazarian A., 2003, JQSRT, 79-80, 881
Lazarian A., Goodman A. A., Myers P. C., 1997, ApJ, 490, 273
Li C.-Y., et al., 2021, RAA, 21, 068
Lindegren, L. et al., 2021, A&A, 649, A2
Lombardi M., Alves J., 2001, A&A, 377, 1023
Lombardi M., Alves J., Lada C. J., 2006, A&A, 454, 781
Lombardi M., Lada C. J., Alves J., 2008, A&A, 489, 143
Lombardi M., Alves J., Lada C., 2011, A&A, 535, A16
Lyngå G., 1985, in The Milky Way Galaxy. pp 143–144
Mahalanobis P., 1936, Proc. Natl. Inst. Sci. India, 12, 49
Marigo P., et al., 2017, ApJ, 835, 77
Marraco H., Vega E., Vrba F., 1993, AJ, 105, 258
Martin P., 1974, ApJ, 187, 461
McLachlan G., Peel D., 2000, Finite Mixture Models
McMillan R., 1978, ApJ, 225, 880
Medhi B. J., Maheswar G., Brijesh K., Pandey J. C., Kumar T. S., Sagar R., 2007, MNRAS, 378, 881
Medhi B. J., Pandey J., Kumar T., Sagar R., 2008, MNRAS, 388, 105
Medhi B. J., G. M., Pandey J. C., Tamura M., Sagar R., 2010, MNRAS, 403, 1577–1591
Meingast S., Lombardi M., Alves J., 2017, A&A, 601, A137
Mel'nik A. M., Dambis A. K., 2017, MNRAS, 472, 3887
Meyer M. R., Calvet N., Hillenbrand L. A., 1997, AJ, 114, 288
Monteiro H., Dias W. S., 2019, Monthly Notices of the Royal Astronomical Society, 487, 2385
Monteiro, H. Dias, W. S. Caetano, T. C. 2010, A&A, 516, A2
Monteiro H., Dias W. S., Moitinho A., Cantat-Gaudin T., Lépine J. R. D., Carraro G., Paunzen E., 2020, MNRAS, 499, 1874
Morrissey P., et al., 2007, ApJS, 173, 682

Netopil M., Oralhan İ. A., Çakmak H., Michel R., Karataş Y., 2022, MNRAS, 509, 421
Noormohammadi M., Ghomi M. K., Haghi H., 2023, MNRAS, pp 3538–3554
Orsatti A. M., Vega E. I., Marraco H. G., 2006, AJ, 132, 1783
Orsatti A. M., Feinstein C., Vega E. I., Vergne M. M., 2007, A&A, 471, 165
Pandey A. K., Sharma S., Upadhyay K., Ogura K., Sandhu T. S., Mito H., Sagar R., 2007, PASJ, 59, 547
Pera M. S., Perren G. I., Moitinho A., Navone H. D., Vazquez R. A., 2021, A&A, 650, A109
Perren, G. I. Vázquez, R. A. Piatti, A. E. 2015, A&A, 576, A6
Perren G. I., Pera M. S., Navone H. D., Vázquez R. A., 2022, A&A, 663, A131
Pilbratt, G. L. et al., 2010, A&A, 518, L1
Piskunov A., Kharchenko N., Röser S., Schilbach E., Scholz R.-D., 2006, A&A, 445, 545
Poglitsch A., et al., 2010, A&A, 518, L2
Raboud D., Mermilliod J. C., 1998, A&A, 333, 897
Ramaprakash, A. N. Gupta, R. Sen, A. K. Tandon, S. N. 1998, A&AS, 128, 369
Rautela B., Joshi G., Pandey J., 2004, Bull. Astron. Soc. India, 32, 159
Rieke G. H., Lebofsky M. J., 1985, ApJ, 288, 618
Riello, M. et al., 2021, A&A, 649, A3
Sánchez Almeida J., Allende Prieto C., 2013, ApJ, 763, 50
Sanders W., 1971, A&A, 14, 226
Sarro L., et al., 2014, A&A, 563, A45
Schmidt G. D., Elston R., Lupie O. L., 1992, AJ, 104, 1563
Serkowski K., 1973, IAU Symp., 52, 145–152
Serkowski K., Mathewson D., Ford V., 1975, ApJ, 196, 261
Sheikh A. H., Medhi B. J., 2024, MNRAS, 528, 7037
Singh S., Pandey J. C., Yadav R. K. S., Medhi B. J., 2020, AJ, 159, 99
Skrutskie M. F., et al., 2006, AJ, 131, 1163
Spina L., et al., 2021, MNRAS, 503, 3279
Spitzer Jr L., 1969, ApJ, 158, L139
Spitzer Jr L., Tukey J. W., 1951, ApJ, 114, 187
Stott J. J., 2018, A&A, 609, A36
Subramaniam A., Sagar R., 1999, AJ, 117, 937
Subramaniam A., Gorti U., Sagar R., Bhatt H. C., 1995, A&A, 302, 86
Tang J., Bressan A., Rosenfield P., Slemer A., Marigo P., Girardi L., Bianchi L., 2014, MNRAS, 445, 4287
Tarricq, Y. Soubiran, C. Casamiquela, L. Castro-Ginard, A. Olivares, J. Miret-Roig, N. Galli, P. A. B. 2022, A&A, 659, A59
Vasilevskis S., Klemola A., Preston G., 1958, AJ, 63, 387
Vega E., Orsatti A., Marraco H., 1994, AJ, 108, 1834
Voshchinnikov N., 2012, JQSRT, 113, 2334
Weaver R., McCray R., Castor J., Shapiro P., Moore R., 1977, ApJ, 218, 377
Whittet D., 1977, MNRAS, 180, 29
Whittet D., Van Breda I., 1978, A&A, 66, 57
Whittet D., Martin P., Hough J., Rouse M., Bailey J., Axon D., 1992, ApJ, 386, 562
Wilking B., Lebofsky M., Martin P., Rieke G., Kemp J., 1980, ApJ, 235, 905
de Geus E. J., 1991, in Janes K., ed., Astronomical Society of the Pacific Conference Series Vol. 13, The Formation and Evolution of Star Clusters. pp 40–54
van Marle, A. J. Meliani, Z. Marcowith, A. 2015, A&A, 584, A49

APPENDIX A: VARIABLE STARS, RED GIANTS, BLUE STRAGGLERS AND BE STARS NEAR NGC 1912

Table A1. Variable Stars, Red Giants (RG), Blue Stragglers (BS) and Be Stars near NGC 1912

.

Sl. No.	*Gaia* ID [a]	RAJ2000 (°)	DECJ2000 (°)	G mag	$G_{BP} - G_{RP}$ mag	MP(CG18)	MP(This Work)	TYPE
				Variable Stars [b]				
1	Gaia DR3 183369131876677632 (V1)	81.94208	36.04202	13.96	0.83	0.8	0.18	γ Dor
2	Gaia DR3 184120304475261056 (V2)	81.90277	36.12965	14.02	0.86	0.5	0.13	γ Dor
3	Gaia DR3 183273646164503040 (V3)	82.27619	35.57744	13.83	0.77	0.5	0.18	γ Dor
4	Gaia DR3 183339926099331072 (V4)	82.05748	35.86597	13.88	0.82	1	0.39	γ Dor
5	Gaia DR3 183347480943471872 (V5)	82.25256	35.79463	13.79	0.75	0.8	0.70	γ Dor
6	Gaia DR3 184094294153404160 (V6)	81.77620	35.96430	13.74	0.78	-	-	γ Dor
7	Gaia DR3 184120613712883840 (V7)	81.97674	36.15572	12.40	0.81	-	-	γ Dor
8	Gaia DR3 183365283586177664 (V8)	82.06577	36.00430	13.94	0.84	-	-	δ Scuti
9	Gaia DR3 183353940574561152 (V9)	82.22058	35.98504	13.44	0.86	-	-	δ Scuti
10	Gaia DR3 183330477171446144 (V10)	81.82604	35.63284	12.03	0.93	-	-	δ Scuti
11	Gaia DR3 183358132464038400 (V11)	82.46541	36.04251	12.75	0.66	-	-	δ Scuti
12	Gaia DR3 183293712252780032 (V12)	82.51487	35.58791	12.26	0.63	-	-	δ Scuti
13	Gaia DR3 183337654058223360 (V13)	81.97456	35.76444	13.26	0.87	-	-	δ Scuti
14	Gaia DR3 183365970780899072 (V14)	82.17354	36.02031	13.62	0.71	0.5	0.70	δ Scuti
15	Gaia DR3 183353498195886720 (V15)	82.23666	35.93907	15.19	1.05	-	-	δ Scuti
16	Gaia DR3 183320680347061888 (V16)	82.05980	35.59108	16.17	1.31	-	-	EW
17	Gaia DR3 183314534252826624 (V17)	82.01217	35.53690	16.68	1.42	-	-	EW
18	Gaia DR3 183325387630106496 (V18)	81.96429	35.72203	14.43	1.13	-	-	EW
19	Gaia DR3 183345939053525504 (V19)	82.29913	35.72207	15.42	1.15	-	-	EW
20	Gaia DR3 184098554760945024 (V20)	81.72832	36.04424	14.53	1.61	-	-	EA
21	Gaia DR3 183274470798227200 (V21)	82.25080	35.58982	15.56	1.39	-	-	EA
22	Gaia DR3 183275153693857408 (V22)	82.26192	35.63772	15.91	1.19	-	-	EA
23	Gaia DR3 183315388946195328 (V23)	81.83070	35.63772	12.53	0.76	-	-	γ Dor
24	Gaia DR3 183327930250733440 (V24)	82.07234	35.82011	13.37	2.96	-	-	unknown
				Other Stars[c]				
25	Gaia DR3 183347893258722816 (74)	82.25560	35.84683	10.94	0.33	0.6	0.44	Be
26	Gaia DR3 183327380494927104 (124)	82.03980	35.77309	10.47	0.54	-	-	Be
27	Gaia DR3 183327694032493952 (133)	82.07677	35.80000	10.27	0.30	0.8	-	Be
28	Gaia DR3 183349340667565696 (70)	82.28490	35.85825	9.39	1.40	0.5	0.31	RG
29	Gaia DR3 183349684264914816 (194)	82.34628	35.88638	8.11	1.21	-	-	RG
30	Gaia DR3 183365627183540224 (292)	82.16576	35.97469	9.43	1.44	-	-	RG
31	Gaia DR3 183325353270369152 (370)	81.94623	35.71090	9.27	1.82	-	-	RG
32	Gaia DR3 183347244723585536 (11)	82.20296	35.79145	10.60	0.41	0.6	0.73	BS

[a] IDs in the parentheses are taken from the original works of [b] Li et al. (2021) and [c] Høg et al. (2000).